PHYSICAL REVIEW B **99**, 014207 (2019)

Heat and charge transport in bulk semiconductors with interstitial defects

Vitaly S. Proshchenko,[1] Pratik P. Dholabhai,[1] Tyler C. Sterling,[2,1] and Sanghamitra Neogi[1,*]
[1]*Ann and H. J. Smead Aerospace Engineering Sciences, University of Colorado, Boulder, Colorado 80309, USA*
[2]*Materials Science and Engineering, University of Colorado, Boulder, Colorado 80309, USA*

(Received 29 May 2018; revised manuscript received 12 November 2018; published 22 January 2019)

Interstitial defects are inevitably present in doped semiconductors that enable modern-day electronic, optoelectronic, or thermoelectric technologies. Understanding the stability of interstitials and their bonding mechanisms in the silicon lattice was accomplished only recently with the advent of first-principles modeling techniques, supported by powerful experimental methods. However, much less attention has been paid to the effect of different naturally occurring interstitials on the thermal and electrical properties of silicon. In this work, we present a systematic study of the variability of heat and charge transport properties of bulk silicon, in the presence of randomly distributed interstitial defects (Si, Ge, C, and Li). We find through atomistic lattice dynamics and molecular dynamics studies that interstitial defects scatter heat-carrying phonons to suppress thermal transport—1.56% of randomly distributed Ge and Li interstitials reduce the thermal conductivity of silicon by ∼30 and 34 times, respectively. Using first-principles density functional theory and semiclassical Boltzmann transport theory, we compute electronic transport coefficients of bulk Si with 1.56% neutral Ge, C, Si, and Li interstitials, in energetically favorable hexagonal, tetrahedral, split-interstitial, and bond-centered sites. We demonstrate that hexagonal-Si and hexagonal-Ge interstitials minimally impact charge transport. As an illustration of the relevance of this work for practical applications, we predict the thermoelectric property of an experimentally realizable bulk Si sample that contains Ge interstitials in different symmetry sites. Our research establishes a direct relationship between the variability of structures dictated by fabrication processes and heat and charge transport properties of silicon. The relationship provides guidance to accurately estimate performance of Si-based materials for various technological applications.

DOI: 10.1103/PhysRevB.99.014207

I. INTRODUCTION

Applicability of any material to optical, energy transport, or topological architectures is largely determined by our ability to design and manipulate defects and doping in the material, which either supply or destroy free carriers. Significant advances have been made to understand the physics and the properties of defects in inorganic semiconductors, owing to the strong historical interaction between the theory of defects and doping-enabled semiconductor-based technologies—microelectronics [1–4], photovoltaics [5], light-emitting diodes (LEDs) [6], and more recently, spintronics [7] and quantum devices [8,9]. The design of defect-tolerant semiconductors that can retain their properties despite the presence of crystallographic defects is actively being pursued for the next-generation Earth-abundant solar energy conversion technologies [10]. In contrast, introduction of defect-induced innovative transport mechanisms in bulk [11,12] and nanostructured materials [13–16] enabled paradigm-shifting advances in the thermoelectric (TE) energy conversion devices. Innovative defect engineering efforts in future technology-enabling materials heavily rely on a better understanding of the role of intrinsic point defects in carrier transport.

In the last two decades, Si-Ge-based heterostructures have emerged as key materials in numerous electronic, optoelectronic [17–19], and TE devices [20–23]. During the growth and fabrication of these devices, especially ones that require high-temperature processes, several undesirable damages [24]—vacancies, interstitials, additional substitutional atoms, clusters—are introduced as a by-product [25]. These defects mostly degrade the device performances [26,27]. It is of great technological significance to consider the variability of the configurations, dictated by fabrication processes, while predicting the performance of Si-based materials for various applications. Additionally, with the advent of space exploration missions, Si electronics are being exposed to a variety of energetic particles and photons. Energetic particles tend to impart displacement damages in the material by modifying the local lattice structure and creating crystalline defects and interstitial-vacancy complexes [24]. The resulting effects may manifest as transient changes or as long-term parametric degradation in the performance of the devices. Therefore, understanding the effects of radiation on electronic devices and circuits is particularly important for the microelectronics in space applications. However, it is very hard to quantify the extent of degradation of the electronic and heat dissipation properties of the semiconductor material due to the displacement damages, caused by radiation.

Studies of point defects in Si, introduced through fabrication-induced damage, started in the late 1940s [24]. However, a unified understanding of the stability of

---

[*] sanghamitra.neogi@colorado.edu

interstitial defects and their formation mechanisms was accomplished only recently, with the advent of first-principles modeling techniques [28–33], supported by powerful experimental methods, such as electron paramagnetic resonance spectroscopy and deep-level transient spectroscopy [34–38]. The commonly studied interstitials in the silicon lattice, using first-principles modeling methods, are self-interstitials [29,30,39–41], germanium [33,40], carbon [42–44], and lithium [45–47]. Isolated carbon interstitials have been identified as one of the dominant stable defects in irradiated high-purity silicon [35]. C-interstitial defects arguably are formed when a mobile Si self-interstitial (e.g., generated by irradiation or ion implantation), reacts with a substitutional C impurity in an exothermic kick-out process [44]. Investigation of C interstitials thus provided an indirect route to inspect the configuration and the properties of Si self-interstitials, which were extensively investigated [48]. Furthermore, interstitial defects provide important clues regarding solubility, diffusion, and migration of one element into another as well as structural properties, such as strain in a material. One important problem encountered in improving present-day electronic devices is that the diffusion of dopant atoms often limits how small the devices can be made. This is especially challenging for highly doped samples. Dopant diffusion is arguably mediated by vacancies and interstitials, introduced during fabrication, and is termed "transient enhanced diffusion" (TED). It is crucial to acquire a good understanding of vacancy and interstitial defects in silicon to minimize TED. Diffusion of Li and Ge interstitials in bulk Si has been experimentally studied at high temperatures [49,50]. The role of interstitial defects as mediators of the diffusion mechanisms in Si and Ge has been highlighted experimentally and by first-principles calculations [33,51,52] Lastly, Li interstitials in silicon significantly influence the stability of the host material, and thus, the applicability of silicon as an anode material in the next-generation lithium-ion batteries. The energetics and dynamics of Li insertion into covalently bonded Si are critical in determining key performance parameters such as voltage profile, power rate, temperature effects, safety, and cyclability in the next-generation lithium-ion batteries [47]. The presence of isolated Si atoms, SiSi clusters, and Li interstitials in Si leads to amorphization of crystalline Si at room temperatures [47]. However, what impacts these defects have on the overall performance of the battery remains to be established. The first-principles-based electronic structure modeling studies cited in this paragraph primarily investigated the structural changes, stability, and bonding mechanism of defects in the silicon lattice. The impact of these interstitial defects on electronic properties, however, still remains to be determined, as only a few studies exist that calculated electronic transport properties in the presence of point defects.

Introduction of vacancies and substitutional point defects have been extensively investigated to suppress the thermal conductivity (TC) of bulk silicon [53–55]. Around a vacancy, lattice relaxation creates additional scattering sites for phonons. The reduction of TC was thus explained by increased phonon scattering and a reduction in the mean-free path (MFP) of phonons, due to the relatively high concentration of vacancies (1–4 %) [55–57]. However, the number of studies that investigated the influence of interstitials on TC is fairly limited. Few studies exist that focused on phonon properties employing Green's function techniques with approximated force constant based models [58–62]. Interstitials in the context of thermoelectrics have been widely studied in the form of clathrates and other caged structures [63]. However, a comprehensive understanding of the effect of different naturally occurring interstitials (Si, Ge, C, and Li) on the thermal and electrical properties of silicon does not exist. In this work, we present a systematic study of the variability of charge and heat transport properties of bulk silicon in the presence of randomly distributed interstitial defects (Si, Ge, C, and Li) using first-principles density functional theory (DFT), atomistic lattice dynamics and equilibrium (EMD), and nonequilibrium molecular dynamics (NEMD). This theoretical investigation furnishes indirect measures to estimate the presence of interstitial defects in a sample. Furthermore, our study establishes a processing-structure-transport (heat and charge) property map that provides guidelines for design, synthesis, and processing, to develop Si-based materials with predictable, robust, and optimal performance.

As an illustration of the relevance of this work for practical applications, we discuss the relationship between structure of silicon with naturally occurring interstitial defects, dictated by processing, and its performance for thermoelectric applications. Solid state TE generators [64] are expected to play a key role to meet the rapidly increasing power demands of the internet of things, by converting any source of heat into electricity. Defect engineering in TE materials aims to affect the interdependent heat and charge transport properties toward higher material performance. The maximum power-generation efficiency (η) of a TE material is $\eta = (\frac{T_{\text{hot}}-T_{\text{cold}}}{T_{\text{hot}}})[\frac{\sqrt{1+ZT}-1}{\sqrt{1+ZT}+(\frac{T_{\text{cold}}}{T_{\text{hot}}})}]$, where the ratio of the temperature difference between the hot and the cold end ($T_{\text{hot}} - T_{\text{cold}}$) to T_{hot} is the Carnot efficiency. The dimensionless figure of merit, ZT, is the primary parameter that determines TE efficiency and is given by $ZT = \frac{\sigma S^2 T}{\kappa_e+\kappa_{ph}} = \frac{\text{PF}\ T}{\kappa_e+\kappa_{ph}}$, where σ is the electrical conductivity, S is the thermopower or Seebeck coefficient, T is the temperature, PF ($= \sigma S^2$) is the power factor, and κ_e and κ_{ph} are the electronic and ionic contributions to the TC, respectively [64]. Our MD studies show that interstitial defects scatter heat-carrying phonons to suppress the κ_{ph}; 1.56% of randomly distributed Li, Ge, Si, and C interstitials reduce the TC of silicon by ~34, 30, 20, and 9 times, respectively. We provide insights into the modification of phonon propagation properties of large experimentally realizable Si systems in the presence of randomized interstitial defects, by computing the density of states and group velocities using lattice dynamics techniques and the frequency-dependent phonon MFPs, employing a newly developed method based on NEMD [65–67]. We show the implementation of the newly developed method to verify Rayleigh scattering by interstitial defects [68]. Defects commonly introduce additional impurity levels within the TE material's energy band gap [69,70], leading to a reduced charge transport. We investigate the electronic transport properties of bulk Si with 1.56% Ge, C, Si, and Li interstitials in hexagonal, tetrahedral, split-interstitial, and bond-centered sites. We demonstrate that Si and Ge interstitials in the hexagonal sites minimally impact the charge transport properties of bulk silicon. This combined with the decreased values of κ_{ph} leads

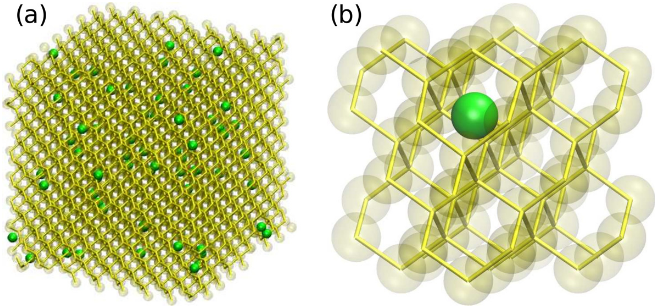

FIG. 1. Representative configurations of bulk Si with Ge interstitials studied using (a) classical MD and (b) first-principles DFT method. The MD configuration consists of 4096 host Si (yellow) and 64 interstitial Ge (green) atoms. The DFT configuration has 64 Si (yellow) and 1 Ge (green) atoms. The concentration of Ge in bulk Si is 1.56% in both configurations.

to a 14 and 17 times improved ZT, respectively. To complete the study, we model and predict the thermoelectric property of an experimentally realizable bulk silicon sample with Ge interstitials in different symmetry locations.

II. METHOD

In this section, we provide the details of the systems we investigated, and the first-principles and the atomistic numerical methods we employed, to elucidate the impact of interstitial defects on electronic and heat transport properties of bulk silicon.

A. System details

We investigated bulk silicon configurations with commonly occurring interstitial impurities: Ge, C, Si, and Li; the systems studied will henceforth be referred to as Si-I-X systems (where $I \equiv$ interstitials and $X =$ Ge, C, Si, or Li). Representative microscopic configurations of the Si-I-X systems investigated are shown in Fig. 1. The bulk Si supercell templates were generated by replicating a conventional unit cell (CC) of silicon, which consists of 8 atoms in a diamond face centered cubic lattice arrangement with side length 5.431 Å. The guest atom species (X) were then inserted in the interstitial sites (I) of these supercell templates to create the Si-I-X configurations. The occurrence of Ge, C, Si, and Li interstitial defects have been discussed in multiple past studies [33,35,44,48,50]. The most widely studied interstitial sites in bulk silicon lattices, investigated with semiempirical and first-principles methods, are of hexagonal, tetrahedral, split-interstitial, and bond-centered type [29,30,33,39,40,42,43,45,46]. Previous studies discussed that different interstitial atoms occupy different energetically favorable sites in the silicon lattice. We include a discussion about the formation energies of these defects in Sec. III E. Additionally, stability of interstitials also depends on the charge state of the defects due to the change in the number of dangling bonds, as discussed in the literature [28,30,32,71–73]. The focus of the first-principles studies has mainly been on effective calculation of formation energies [32] and defect levels within the band gap [74]. However, the problem of accurately calculating dispersion of interstitial defect levels with DFT, especially in the correct charged state, remains open. It has been argued that correct defect levels in the band diagram can only be obtained by augmenting Kohn-Sham theory with *ad hoc* procedures (e.g., semiempirical scissors correction) [75]. Recent studies suggested some improvements in the method that yielded better predictions for defect formation energies; however, no direct method exists that can generate the band dispersion for a charged interstitial, required for electronic transport property estimation, to the best of our knowledge. Besides, self-interstitials are reported to be stable in a $\mathrm{Si}^{(0)}$ charge state in highly doped n-type Si, which we are mainly investigating in this work [35,73]. Self-interstitials in p-type silicon are argued to be stable in a tetrahedral site with $\mathrm{Si}^{(+2)}$ charge state [73]. The studies investigating charge states of C, Ge, and Li interstitials in Si are extremely limited in number. Few studies were performed focusing on isolated neutral Ge, featuring a diluted limit that did not incorporate the effect of charge accumulation. Investigation of the variation of electronic transport properties with interstitials in different charge states is out of the scope of the present study.

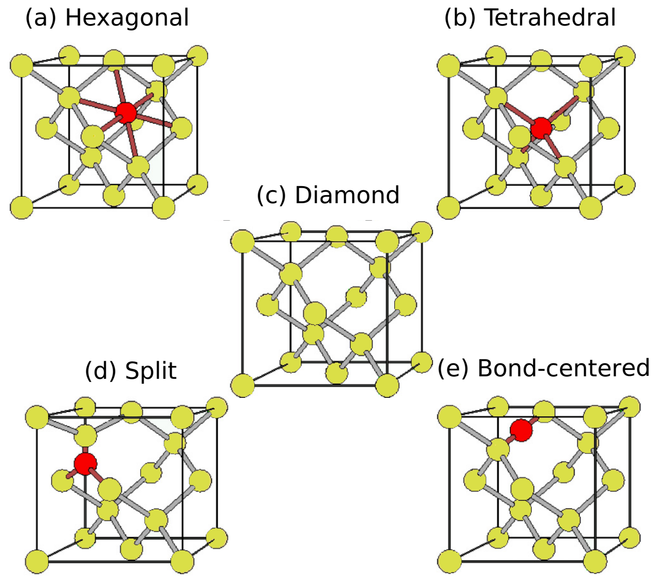

FIG. 2. (c) Conventional unit cell of bulk silicon and commonly studied interstitial sites [(a), (b), (d), and (e)] in the diamond cubic lattice. Yellow and red colors represent host and interstitial atoms, respectively.

We investigate electronic transport properties of relaxed Si-I-X configurations with neutrally charged interstitials in each of these previously mentioned energetically stable sites (illustrated in Fig. 2) using DFT. Each of the $[2 \times 2 \times 2] \times$ CC DFT model supercell configurations (Fig. 1) contains 64 Si and 1 interstitial (I) atoms, yielding a 1.56% concentration of guest atoms in host Si. The system size was chosen to allow us to study charge transport in a large set of defected semiconductor systems with a varied chemical bonding environment. We have extensively checked the structural relaxation of atoms around the interstitial atom in our 65-atom supercell and further checked that the atoms far from the defect are nearly in their ideal fcc diamond lattice positions. Our analysis combined with insight from the literature [76] gives us the confidence that use of a 65-atom supercell is justified to perform this study. We acknowledge that the relatively small supercell size does not allow us to model random defect distributions present in fabricated samples. Our DFT model contains uniformly distributed defects only. However, it is well established that computational expenses determine the size limit of systems investigated with DFT. Computational expense is the limiting factor especially since we have investigated a range of systems with different interstitials in multiple different symmetry locations. We tried to capture the effect of random defect distribution with our MD studies instead. We performed MD studies of the Si-I-X systems with three different interstitial concentrations, 0.1%, 0.5%, and 1.56%, to study the extent of disruption of phonon transport in the presence of randomly distributed interstitial scatterers. The MD models consisted of several thousands of atoms ($\geqslant 32\,768$). The system sizes were chosen to represent bulk systems with low enough interstitial concentrations realizable in experimental conditions [23], as well as to perform a large set of calculations with reasonable computing expenses. The interstitial sites in these large replicated MD supercells were generated using a systematic search algorithm. The algorithm employs a repulsive pair potential to model interatomic interactions between an interstitial atom and its neighboring host lattice atoms to identify interstices in materials [77]. This algorithm primarily yields the information about tetrahedral sites in a Si-I-X supercell. These generated tetrahedral sites were randomly populated with a chosen number of interstitial atoms, consistent with the concentration. We obtain the initial configurations of the Si-I-X systems by placing all the different species investigated (Ge, C, Si, and Li) at tetrahedral interstitial sites, to ensure a consistent comparison of their impact on thermal properties of bulk Si. However, as we discuss in the following "Atomistic calculations" subsection, a percentage of these interstitial atoms are likely to populate other sites in the final configurations, following equilibration at 300 K, due to thermal fluctuations. We investigate thermal conductivities of three distinct randomized configurations for each interstitial (X) concentration with EMD. However, we compute length-dependent phonon transmission and MFPs in only one configuration for each of the chosen length systems of our considerably larger 1.56% Si-I-Ge NEMD models (~600 000 atoms), due to the large computational expenses.

B. Atomistic calculations

We analyzed the thermal transport properties of Si-I-X systems by performing EMD simulations, with periodic boundary conditions enforced in all three directions to emulate infinite systems. The interatomic forces between Si, Ge, and C atoms were modeled using the empirical potential proposed by Tersoff [78]. This potential was parametrized to treat heteronuclear bonds, and to reproduce correctly the elastic properties of silicon, SiC, and its defects, in particular. To model interactions in the Si-I-Li systems, we implemented a second-nearest-neighbor modified embedded atom method (2NN MEAM) interatomic potential, which was used to describe interactions in Li-Si alloys [79]. To the best of our knowledge, this potential has not been employed for thermal property calculations. We performed several test calculations to obtain TC of bulk Si with the 2NN MEAM potential, and compared with the TC results obtained with the widely used Tersoff potential. We present the computational details and the comparison in the following paragraphs.

All systems with interstitials were equilibrated at 300 K to ensure that the stability of the structures is maintained. After equilibration, initial velocities in the MD simulations were set to 300 K and the systems were coupled to a Nosé–Hoover thermostat for 1 ns, to decorrelate the systems from their initial configurations. The thermostat was then decoupled from the systems so that the simulations were performed under microcanonical conditions. The equations of motions were integrated with a time step of 0.25 fs to ensure energy conservation over simulation times of several tens of nanoseconds. We computed the TCs from the fluctuations of the heat current in EMD simulations, using the Green-Kubo relation [80]: $\kappa_\alpha = 1/(k_B V T^2) \int_0^\infty dt \langle J_\alpha(t) J_\alpha(0)\rangle$ where $\alpha = x, y, z$; k_B is the Boltzmann constant, V is the volume of the system, T is the temperature, and $\langle J_\alpha(t) J_\alpha(0)\rangle$ is the heat current autocorrelation function along the direction (α) of heat propagation. The heat current is computed by $\mathbf{J} = \sum_i^N \epsilon_i \mathbf{v}_i + \frac{1}{2} \sum_{i,j;i\neq j}^N (\mathbf{F}_{ij} \cdot \mathbf{v}_i)\mathbf{r}_{ij} + \frac{1}{6} \sum_{i,j,k;i\neq j;j\neq k}^N (\mathbf{F}_{ijk} \cdot \mathbf{v}_i)(\mathbf{r}_{ij} + \mathbf{r}_{ik})$, where ϵ_i and $\mathbf{v}_i$ are the energy density and velocity associated with atom i, respectively. $\mathbf{F}$ is the interatomic force acting between atoms separated by a distance $\mathbf{r}$. The heat flux data were recorded at 5 fs intervals. Total simulation times varied between 15 and 30 ns for different configurations. All EMD simulations were carried out using LAMMPS software [81].

A known disadvantage of the Green-Kubo formalism combined with the EMD method is that the TCs obtained might suffer from system size dependence. The size-converged TC value of bulk Si modeled with the Tersoff empirical potential is reported to be 196.8 ± 33.3 W/(m K) [82]. However, no such study has been reported for Si described with the 2NN MEAM interatomic potential [79]. To obtain a reference bulk Si TC described with the 2NN MEAM interatomic potential, we performed simulations of supercells of increasing volume from $[4 \times 4 \times 4] \times$ CC to a size $[32 \times 32 \times 32] \times$ CC containing 262 144 atoms. As depicted in Fig. 3, we find that the converged bulk Si TC using 2NN MEAM is 122.22 ± 13.81 W/(m K). We will use this value in the following analysis as our reference for TC of bulk Si, modeled using the 2NN MEAM empirical potential. We find that to obtain a converged value of TC, one has to use simulation cells with at least 32 768 atoms. Each of the data points reported in Fig. 3 was obtained by averaging over 10 calculations performed with independent configurations, and the standard deviation is reported as the uncertainty. Compared to the experimentally measured TC values (depicted in the blue shaded regions in Fig. 3) ranging from 130 to 150 W/(m K) at 300 K, it can be argued that the bulk Si TC modeled using 2NN MEAM is in reasonable agreement with the measured values, and the empirical potential offers a rational choice to model bulk Si with Li interstitials.

In order to test system size dependence of TCs of Si-I-X samples, we computed TCs of two systems, Si-I-Ge and Si-I-Li, each with two supercells of sizes $[8 \times 8 \times 8] \times$ CC (4096 atoms) and $[16 \times 16 \times 16] \times$ CC (32 768 atoms). This

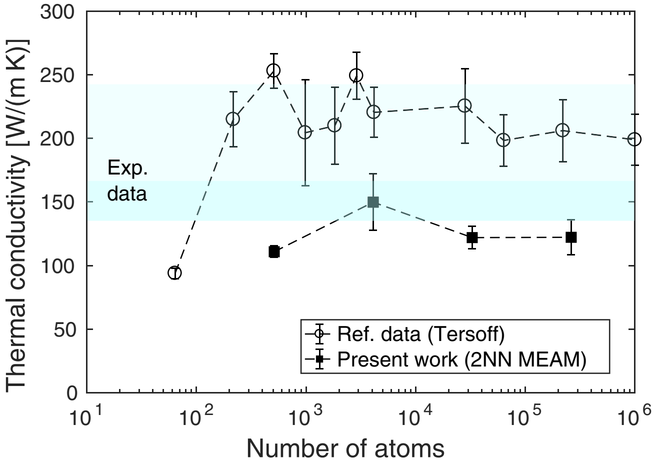

FIG. 3. Thermal conductivities of bulk silicon at 300 K as a function of the number of atoms in the simulation cell, computed from equilibrium molecular dynamics using the Green-Kubo theorem. The filled squares represent the TCs computed using the 2NN MEAM potential [79]. To facilitate a coherent comparison, corresponding TCs obtained with Tersoff potential [82] are shown with open circles [data extracted from Ref. [82]; converged TC: 196.8 ± 33.3 W/(m K)] alongside 2NN MEAM values. The dashed line connecting the points represents a guide to the eye. The blue shaded region, extracted from Ref. [82], indicates the range of TCs measured in the experiments where most values lie in the darker shaded region. The converged TC of bulk Si using 2NN MEAM is 122.22 ± 13.81 W/(m K).

strategy ensured that we tested the size convergence of TCs of defected Si systems described with two different potentials used in this study, Tersoff and 2NN MEAM. For the two system sizes of Si-I-Ge and Si-I-Li, the TCs differ by ~9.8% and ~9.6%, respectively, which fall within our method of uncertainty limits. In our conservative estimate, the dimensions of the simulation supercell with minimum system size effects are $[16 \times 16 \times 16] \times$ CC. Henceforth, all TC computations of Si-I-X systems were performed using this system size. For each of the three chosen concentrations of interstitials (0.1%, 0.5%, and 1.56%) in the Si-I-X systems, TCs are averaged over 45 data sets—obtained from 3 randomized configurations, simulations initialized with 5 different random velocities, and results averaged over x, y, and z directions.

C. Nonequilibrium molecular dynamics simulations

We computed phonon transmission functions and MFPs in bulk Si and Si-I-X systems by analyzing atom trajectories obtained from NEMD simulations. We implemented a recently developed method by Sääskilahti *et al.* [66,67,83] to perform the analysis. This method allows us to take anharmonic effects into account at a reasonable computational cost. Due to the large computational expenses required for this analysis, we only investigated Si-I-Ge systems with 1.56% Ge interstitials, to discuss phonon scattering from interstitials and quantify the subsequent impact on thermal transport. The interatomic forces between Si and Ge were modeled using the Tersoff empirical potential, parametrized to treat heteronuclear bonds [78]. The equations of motions were integrated using the LAMMPS package [81] with a time step of 0.5 fs.

All Si-I-Ge systems were relaxed at 0 K and then equilibrated at 300 K with a Nosé-Hoover thermostat. After equilibration, we imposed finite-temperature differences on the systems, by coupling atoms located within a distance 5.431 nm from the left and the right boundaries of the simulation cells along the x direction, to two Langevin heat reservoirs to rescale atom velocities to $T_{\mathrm{cold}} = T - \frac{1}{2}\Delta T_{\mathrm{NEMD}}$ and $T_{\mathrm{hot}} = T + \frac{1}{2}\Delta T_{\mathrm{NEMD}}$, respectively, with a Langevin damping parameter of 0.5 ps [84]. We computed the frequency-dependent heat current $q(\omega)$ and phonon transmission functions $\mathcal{T}(\omega, L)$ of bulk Si for six different system lengths L (i.e., the region between the reservoirs) 2, 25, 41, 204, 500, and 1000 nm and of Si-I-Ge systems for five different system lengths 2, 25, 41, 204, and 500 nm. We applied $\Delta T_{\mathrm{NEMD}} = 40$ K for $L < 10$ nm, 60 K for $10\ \mathrm{nm} \leqslant L < 500$ nm, and 80 K for $L \geqslant 500$ nm. Atoms at the far left and the far right simulation cell boundaries along the x direction were kept fixed to their equilibrium positions, to eliminate cell drift. Periodic boundary conditions were applied to the cell transverse to the heat flow direction.

This NEMD-based approach is based on computing frequency-dependent heat current $q(\omega)$ across the sample, from the Fourier transform of an auxiliary time correlation function, between the interatomic forces and velocities of atoms:

$$q(\omega) = -\frac{2}{t_{\mathrm{simu}}\omega} \sum_{\substack{i\epsilon\widetilde{L},\, j\epsilon\widetilde{R} \\ \alpha,\, \beta\epsilon\{x,\, y,\, z\}}} \mathrm{Im}\big\langle \hat{v}_i^{\alpha}(\omega)^{*} K_{ij}^{\alpha\beta}\, \hat{v}_j^{\beta}(\omega)\big\rangle, \tag{1}$$

where t_{simu} is the total simulation time, ω is the angular frequency, $K_{ij}^{\alpha\beta}$ is the interatomic force constant, and $\hat{v}_i^{\alpha}(\omega)$ and $\hat{v}_j^{\beta}(\omega)$ are the discrete Fourier transforms of the velocities of atoms i and j, respectively, in directions $\{\alpha, \beta\}\epsilon\{x, y, z\}$. We compute the frequency-dependent heat current $q(\omega)$ through the plane located halfway between the cold and the hot reservoirs, by summing over the pairwise spectral heat current between particles located on opposite sides of this plane. $(\widetilde{L}, \widetilde{R})$ denote the left and right sides of this plane, respectively. The summing is performed over all pairs of atoms within a cutoff distance of 0.54 nm. In solids, the atoms remain close to their average positions and we assume a harmonic approximation of the interatomic forces ($K_{ij}^{\alpha\beta}$) to reduce the cost to compute the pairwise heat currents. This restriction does not, however, mean that effects of anharmonic scattering are neglected, because the NEMD simulations were performed within the fully anharmonic framework [66,84]. The phonon transmission function is then obtained from the spectral heat current as

$$\mathcal{T}(\omega, L) = \frac{q(\omega)}{k_B \Delta T}, \tag{2}$$

where $\mathcal{T}(\omega, L)$ is the dimensionless, bath-to-bath length-dependent transmission function and k_B is the Boltzmann constant. We calculate the spectral decomposition of TC across the plane from

$$\kappa(\omega) = \frac{q(\omega)}{A \nabla T}, \tag{3}$$

where ∇T is the local temperature gradient, determined by linear-fitting the steady-state temperature profile [85]. The simulation times for our configurations varied between 10 ns ($\leqslant$200 nm) and 20 ns ($>$200 nm), to achieve a stationary condition and obtain a linear temperature profile. For each of the systems, 5-ns-long simulations were performed to collect the atom velocities every 5 fs interval, after the system reached a nonequilibrium steady state. The 5-ns-long velocity data were divided into 20 blocks and $q(\omega)$ and $\mathcal{T}(\omega, L)$ are obtained from the averages of these 20 divisions, to eliminate noise from the reported results [86,87]. Additionally, we performed a smoothening of the sharply fluctuating transmission functions by convoluting with a Gaussian window with standard deviation of 0.5 THz.

Assuming diffusive transport, we evaluate the frequency-resolved phonon MFPs $\Lambda(\omega)$ from the ratio between the transmission at a specific length L_1 as a reference and the transmission at other lengths results [66,67,86]:

$$\frac{\mathcal{T}(\omega, L_1)}{\mathcal{T}(\omega, L)} = 1 + \frac{L - L_1}{\Lambda(\omega) + L_1}. \tag{4}$$

Previous studies have shown that TCs predicted by NEMD show size dependence for systems with cross sections up to $[10 \times 10] \times$ CC, transverse to the heat flow, and heat reservoir lengths less than 32 CC [85,88]. However, phonon MFPs in bulk Si can range up to $\sim\mu$m length [89,90]. We simulated systems up to 1 μm of length in the transport direction, to obtain converged results for phonon MFPs of Si. Due to the computational burden imposed for simulating such large structures, we restrict our simulation cell sizes to cross sections of $[6 \times 6] \times$ CC and bath lengths of 10 CC. We checked the dependence of TC on bath length by varying the length from 1 CC to 40 CC. We found that a bath length of 10 units yielded TC within 10% of the converged value and therefore chose our baths to be 10 CC long.

D. First-principles calculations

A century of developments in empirical and semiempirical models [91,92] realized the modern theory of defects in crystalline solids, based on first-principles electronic structure techniques [93]. The method has been demonstrated to expose phenomena that can be readily implemented to optimize the performance of a broad-range of technology-enabling materials. We implemented electronic structure calculations with DFT, using the generalized gradient approximation (GGA) of the exchange-correlation functional by Perdew-Burke-Ernzerhof (PBE) [94] as implemented in the plane wave code Quantum Espresso (QE) [95] to study the effect of interstitial species types and their symmetry positions on electronic transport. We employed scalar relativistic norm-conserving pseudopotentials to treat core electrons of both the host Si and the interstitial atoms [95]. The Kohn-Sham orbitals expanded in terms of a plane wave basis set had a cutoff energy of 30 Ry for all calculations. A convergence threshold for self-consistency was chosen to be 10^{-9}. As illustrated in Fig. 1(b), the periodic DFT supercells consisted of 64 silicon and 1 interstitial atoms—corresponding to 1.56% interstitial concentration in the bulk (see the "System details" subsection for details). The supercells were first relaxed employing the Broyden-Fletcher-Goldfarb-Shanno quasi-Newton algorithm with a $4 \times 4 \times 4$ Monkhorst-Pack k-point mesh [96] to optimize the lattice constants and the atom positions of the Si-I-X supercells. Following relaxation, we performed non-self-consistent field (NSCF) calculations to obtain the band energies using a dense k-point mesh. Such sampling is necessary to converge the calculation of transport coefficients.

The electronic transport coefficients were evaluated within the framework of semiclassical Boltzmann transport theory [68] as implemented in the BoltzTraP code [97]. The code employs Fourier expansion to realize an analytical representation of the band energies, computed with DFT. Using such representations of the electronic band structure and the knowledge of the density of states, one can evaluate the Seebeck coefficient (S), the electrical conductivity (σ), the electronic thermal conductivity (κ_e), and the power factor (PF) ($S^2\sigma$), in the diffusive regime, by integrating the following expressions over the first Brillouin zone [97,98]:

$$\mathcal{L}^{(a)} = \frac{e^2}{V}\int_{BZ}\frac{d^3k}{4\pi^3}\left[\tau(\mathbf{k})v(\mathbf{k})v(\mathbf{k})[\epsilon_{\mathbf{k}} - \mu(T)]^a\left(-\frac{\partial f_\mu}{\partial \epsilon_{\mathbf{k}}}\right)\right], \tag{5}$$

$$\sigma = \mathcal{L}^0, \tag{6}$$

$$S = \frac{1}{eT}\mathcal{L}^1/\mathcal{L}^0, \tag{7}$$

$$\kappa_e = \frac{1}{e^2T}[\mathcal{L}^2 - (\mathcal{L}^1)^2/\mathcal{L}^0], \tag{8}$$

where e is the electron charge and V the volume of the system. The integrand in the expression $\mathcal{L}^{(a)}$ consists of the electron relaxation time $\tau(\mathbf{k})$, the electron group velocity $v(\mathbf{k})$, the ath power of the Kohn-Sham energies $\epsilon_{\mathbf{k}}$ with respect to the electronic chemical potential $\mu(T)$, and the derivative of the Fermi-Dirac distribution function (f_μ). The transport coefficients obtained using Eqs. (5)–(8) are tensors; however since transport is isotropic in the bulk, we report only the trace of S, σ, and κ_e divided by three. Our tests showed that NSCF calculations performed with a $15 \times 15 \times 15$ k-point mesh were sufficient to converge the transport coefficients of the 65-atom Si-I-X systems under investigation.

It is computationally very expensive to compute the electron relaxation time $\tau(\mathbf{k})$ from first principles for our systems. We adopt the constant relaxation time approximation (RTA), which assumes that the relaxation time τ depends only on the carrier concentration and is independent of ϵ and $\mathbf{k}$. With this approximation τ can be factored out of the integrals in Eq. (5), so that it cancels out in the expression of S [Eq. (7)], while it remains as a prefactor in the σ and κ_e expressions [Eqs. (6), (8)]. In RTA τ can be estimated using the experimental values of electron (hole) mobility [99] and effective masses [100], which is known for bulk silicon. We employed the further assumption that a small ($\sim$1%) concentration of interstitials does not affect the electron relaxation times significantly and compute σ and κ_e using τ values obtained from bulk silicon data [99,100]. We acknowledge that this assumption has limited validity. We estimated that 1.56% of substituted Ge decreases electron mobility in silicon by $\sim$4% [76]. However, no such studies exist for interstitial defects making it difficult for us to quantify the effect of interstitials on electron scattering rate. We hypothesize that the same concentration of interstitials would decrease mobility by at least a similar factor ($\sim 4\%$). We further assume that electron relaxation time or scattering rate is independent of symmetry position and atom type of the defects (C, Ge, Si, or Li), and depends on the defect concentration only. This assumption allows us to compare how electronic transport and, as an extension, thermoelectric properties of the Si-I-X systems, with guest interstitials occupying different sites, differ in relation to each other. Within this assumption, we believe that our conclusion about the relative impact of different configurations remains valid, even if the relaxation time or the mobility of electronic carriers in bulk Si is reduced by a factor of 4% or more in the presence of 1.56% interstitial defects. In that case, the overall impact of all configurations studied will be scaled by the appropriate factor.

III. RESULTS AND DISCUSSION

We now turn to discuss the main focus of this work, which is to determine how the presence of interstitials affects heat and charge transport properties of bulk silicon. We performed a series of EMD simulations (see the "Method" section for details) and computed the TCs of Si-I-X systems with varied concentrations of interstitials. After establishing a series of results with MD simulations, we analyzed the bonding environments of the interstitials to characterize their influence on Si lattice structure. To gain insights into the modification of the lattice vibrations of bulk silicon with interstitials, we employed lattice dynamics (LD) and NEMD, and obtained phonon properties of Si-I-X systems. In particular, we computed the vibrational density of states and phonon group velocities with LD and frequency-dependent phonon transmission and MFPs with NEMD in bulk Si with interstitial defects. In parallel, we investigated charge transport properties of a broad range of Si-I-X systems, incorporating various guest species and a number of interstitial symmetry sites for each type. Finally, we combined the phonon and electron transport properties to establish a structure-processing-figure-of-merit map of bulk silicon with interstitials.

A. Thermal conductivity

We start by discussing our MD results. Figure 4 displays the room temperature TCs of Si-I-C (blue squares), -Si (orange inverted triangles), -Ge (green triangles), and -Li (magenta diamonds) systems as a function of interstitial concentrations. The TCs of Si-I-Li systems were computed using the 2NN MEAM potential [79] while the TCs of all the other Si-I-X systems were computed with the Tersoff potential [78]. However, to facilitate a coherent comparison, we scale the reported values in the plot as follows: $\mathrm{TC}^{\mathrm{Li}}_{\mathrm{reported}} = (\mathrm{TC}^{\mathrm{Li}}_{\mathrm{2NN\text{-}MEAM}}/\mathrm{TC}^{\mathrm{Bulk\ Si}}_{\mathrm{2NN\text{-}MEAM}}) \times \mathrm{TC}^{\mathrm{Bulk\ Si}}_{\mathrm{Tersoff}}$ where $\mathrm{TC}^{\mathrm{Bulk\ Si}}_{\mathrm{Tersoff}} = 196.8 \pm 33.3$ W/(m K) [82] and $\mathrm{TC}^{\mathrm{Bulk\ Si}}_{\mathrm{2NN\text{-}MEAM}} = 122.22 \pm 13.81$ W/(m K), respectively. As evident from Fig. 4, the TC is lowered significantly upon the addition of a small fraction of interstitials, for all species types. Remarkably, even with a concentration of 0.1%, there is a $\sim$2 (C)–4 (Li)–fold reduction in the TC from the bulk value [196.8 ± 33.3 W/(m K)]. The decrease in TC is more pronounced with increased interstitial concentrations, as expected. A general trend of decrease in the TC is noted as Si-I-Li < -Ge < -Si < -C, as displayed in Fig. 4, with Ge and Li having the most and C the least impact in lowering the TC, respectively. There is almost a factor 2 difference in the TC between systems with different guest atoms with a small ($\sim$0.1%) concentration of interstitials. The spread in TC decreases with increased concentration of interstitials—randomly dispersed 1.56% Li, Ge, Si, and C interstitials decrease the TC of bulk Si by $\sim$34, 30, 20, and 9 times, respectively. It is interesting to note that the phonon transport in bulk Si is affected significantly more in the presence of Ge interstitials (Fig. 4) than the widely employed Ge substitutions [101] for similar guest species concentrations. This suggests that interstitials offer a strategy to effectively scatter phonons by tuning the mass and the size of the guest atom, and thereby achieve a phonon-glass paradigm to engineer next-generation thermoelectric materials. In the following, we present our analysis on the effect of interstitials on lattice structure and scattering phonons of bulk silicon.

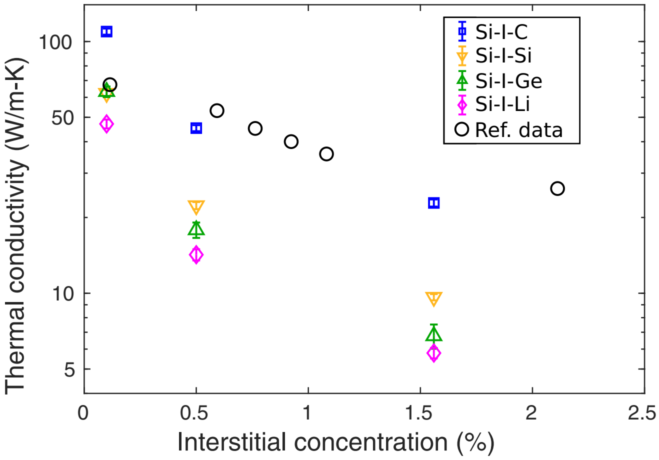

FIG. 4. Thermal conductivities of bulk silicon with C (blue squares), Si (orange inverted triangles), Ge (green triangles), and Li (magenta diamonds) interstitials at 300 K as a function of interstitial concentrations. To offer a comparison with the effect of widely employed Ge substitutions on TC of bulk Si, corresponding TC values are displayed with black open circles (data extracted from Ref. [101]). The x-axis label corresponds to substitutional concentration of Ge in bulk Si in this case.

B. Bonding environment analysis

To understand the influence of interstitials on lattice structure, we analyzed the bonding environment of the guest atoms in the Si-I-X systems. In Fig. 5 we present nearest-neighbor (NN) environment analysis of $[8 \times 8 \times 8] \times$ CC (4096 atoms) Si-I (a) -C, (b) -Si, (c) -Ge, and (d) -Li supercells with 1.56% interstitials. This concentration corresponds to 64 guest interstitials in a Si-I-X supercell. For each guest type, we computed the distance between a given interstitial atom and the eight NN Si atoms, to make sure that we include all first NNs in the analysis. The y axis in Fig. 5 represents the distance between a given interstitial atom and the nearest host Si atoms, while the x axis represents the number of the nth NN

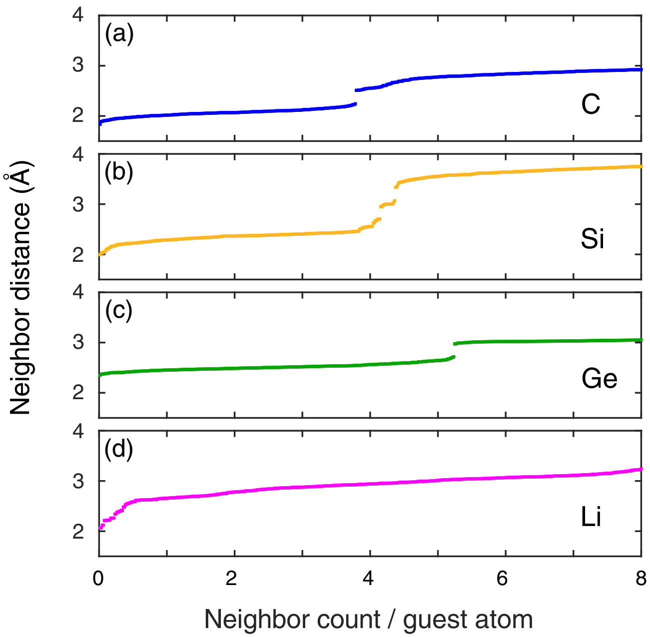

FIG. 5. Nearest-neighbor environment analysis of Si-I (a) -C, (b) -Si, (c) -Ge, and (d) -Li systems. The neighbor distances are sorted in ascending order over all interstitial atoms in the supercell and displayed against the neighbor count.

host atoms within that distance. The neighbor distances are sorted in ascending order over all 64 interstitial atoms in the supercell. A hexagonal interstitial site has a maximum number of first NNs, 6, in the silicon lattice. The tetrahedral, split, and bond-centered interstitial sites have 4, 3, and 2 first NNs, respectively. Different interstitial sites differ by the coordination environment reflected by the number of NNs. Therefore, the number of NNs provides qualitative information about the type of interstitial we have in our system, within thermal fluctuations. From the panels (a), (b), and (c) we mark a gap in the neighbor distance curve and infer that this gap indicates the transition between the first and the second NN distances. The gap reveals information about the average number of first NNs per interstitial atom present in the system, at a given instant. For example, the gap in the case of a C defect [Fig. 5(a)] reveals that this interstitial on average has four first NNs. This corresponds to the tetrahedral site, within thermal fluctuations. The number of the first NNs as well as neighbor distances increase with increasing the size of the interstitial atom (Fig. 5)—average first NN distances in Si-I-C, -Si, and -Ge are estimated as 2.04 ± 0.2 Å, 2.27 ± 0.28 Å, 2.53 ± 0.18 Å, respectively. Additionally, we can qualitatively predict how likely interstitial defects reside in different sites in the lattice by looking at the slope of the curves in Fig. 5. A flatter curve would indicate higher stability in a given interstitial symmetry position, at a given temperature. On the other hand, a steeper curve would indicate a greater variety of defect types since sites with different numbers of NNs have different neighbor distances.

The different number of the first NNs and the uncertainty in the neighbor distances indicate that the interstitials reside in a dynamic bonding environment due to temperature fluctuations. The NN analysis manifests that the interstitials access other symmetry positions during MD simulations even though the initial configurations consisted of only four-coordinated tetrahedral sites. This was the reason to check 8 NN distances in the previous bonding environment analysis as well. An interesting aspect that can be noted from Fig. 5 is that there is no clear separation between the first and the second NN distances in Si-I-Li unlike the other systems investigated. Therefore, we do not report an estimated first-NN value for this system. This disparity illustrates that Li interstitials are more diffusive in character leading to significant disorder in the lattice, which is likely to be the reason for Li interstitials being the most effective in lowering bulk Si TC as compared to Ge, C, or Si. One other likely origin of dissimilar NN environment of interstitial atoms is strain. In these materials, atoms with dissimilar masses and sizes compared to the host atoms (other than Si-I-Si) are randomly placed in interstitial sites, leading to anisotropic strain in the material. The strain could further contribute to disparate relaxation that results in diverse bonding environment of the interstitial atoms, leading to varied impact on TC.

TABLE I. Thermal conductivities of 4096-atom Si supercells with 1.56% Ge and Li interstitial atoms placed uniformly and randomly.

System	Uniform [W/(m K)]	Random [W/(m K)]
Si-I-Ge	11.23 ± 0.48	5.88 ± 0.23
Si-I-Li	5.62 ± 0.88	5.36 ± 0.83

Interstitial atoms serve as scattering centers that hinder thermal transport. It can be argued that the individual atoms as well as the diverse local structural environment caused by distribution of interstitials play a critical role in lowering the bulk Si TC [102]. In order to investigate the effect of distribution of interstitials on TC, we investigated two sets of $[8 \times 8 \times 8] \times$ CC (4096 atoms) Si-I-X supercells with 1.56% Ge and Li interstitials: one set contains configurations in which the interstitials were uniformly placed in tetrahedral sites, and the other contains configurations with randomly populated sites. As shown in Table I, we find that the TCs of the Si-I-Ge-uniform samples are ~2 times higher than the Si-I-Ge-random samples. On the contrary, there is no noticeable difference between the TCs of Si-I-Li-uniform and Si-I-Li-random samples. Our NN analysis shows that the individual bonding environments for the 64 interstitials in the equilibrated (at 300 K) Si-I-Ge-uniform samples are similar within statistical fluctuations. However, that is not the case in Si-I-Li-uniform samples due to the diffusive character of Li in Si; the distribution of interstitials in the equilibrated configurations is no longer uniform. Li atoms diffuse through both the uniform and random sample during equilibration to yield a randomized distribution of local strain in the bulk yielding similar TC. Nevertheless, it is important to note that addition of Ge interstitials considerably lowers TC with reduction comparable to Li, despite lacking the diffusive character. Overall, considering the stability of the material we infer that Ge interstitials offer a promising route to decreasing TC of bulk Si.

C. Phonon properties: VDOS and group velocities

In order to characterize the transformation of Si heat carriers in the presence of interstitials in Si-I-X systems, and to elucidate the TC decrease trend (Ge < Si < C), we carried out a series of lattice dynamics (LD) and NEMD based calculations. First, we present our results from the LD calculations. In a bulk material, TC can be modeled using kinetic theory of thermal diffusion, which relies on an approximated solution of the linearized Boltzmann transport equation. The 3 × 3 TC tensor can be expressed as [68]

$$\kappa_{\alpha\beta} = \frac{1}{V}\sum_{\mathbf{q},\lambda} \hbar\omega_\lambda(\mathbf{q})\frac{\partial n_\lambda(\mathbf{q})}{\partial T} v_{\lambda,\alpha}(\mathbf{q}) v_{\lambda,\beta}(\mathbf{q})\tau_\lambda(\mathbf{q}). \quad (9)$$

Similarly to the expression in Eq. (5), the summation is over all phonon modes in the first Brillouin zone, enumerated by wave vector $\mathbf{q}$ and polarization λ. V is the sample volume, $\hbar$ is the reduced Planck constant, $\omega_\lambda(\mathbf{q})$ is the phonon frequency, $n_\lambda(\mathbf{q})$ is the Bose-Einstein distribution, T is temperature, $v_{\lambda,\alpha}(\mathbf{q})$ is the component of the phonon group velocity vector along the Cartesian direction α, and $\tau_\lambda(\mathbf{q})$ is the phonon lifetime. MFPs of a phonon mode $\Lambda(\omega_\lambda(\mathbf{q}))$ can be expressed as the product of its relaxation time $\tau_\lambda(\mathbf{q})$ and the magnitude of its group velocity $|v_\lambda(\mathbf{q})|$. Previous studies computed eigenfrequencies of localized phonon modes and phonon density of states of Si with interstitial defects (Si, O, C, B, Li) in tetrahedral sites using Green's function techniques [60]. However, only isolated interstitials were considered; therefore, the results cannot be compared with our study. We computed phonon dispersions $\omega_\lambda(\mathbf{q})$ of Si-I-X systems by direct diagonalization of the dynamical matrix of a [8 × 8 × 8] × CC (4096 atoms) supercell with 1.56% randomly dispersed interstitials (as described in the "System details" subsection). The sum in Eq. (9) is implicitly affected by the vibrational density of states (VDOS) of the system; we computed the VDOS of Si-I-X systems by integrating phonon frequencies in the first Brillouin zone, using a 8 × 8 × 8 Monkhorst-Pack mesh of q points [96]. Previous calculation of phonon density of states also reported a shift in the intensity in the high-frequency region, as well as a peak near ∼4 THz. However, only one interstitial defect was considered in this calculation, and simplifying assumptions were made that the interstitials are weakly bound to the host atom, and therefore should not disturb the local symmetry appreciably [58]. We find that there is a slight shift and decrease in the peak intensity at about 15 THz, related to optical modes, as displayed in Fig. 6. However, these modes do not contribute greatly to heat transport.

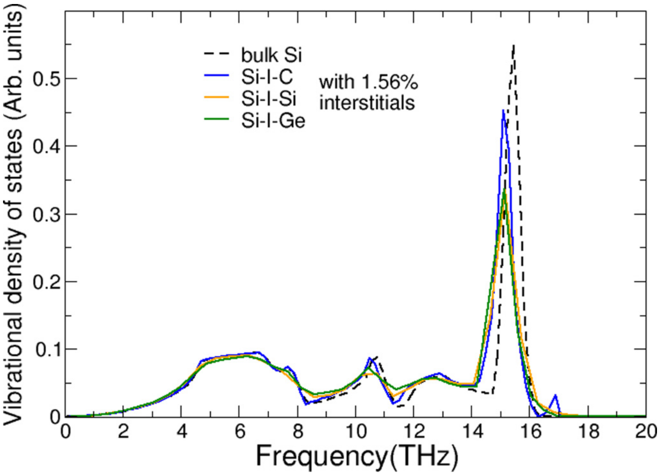

FIG. 6. Vibrational density of states of bulk silicon with 1.56% C (blue), Si (orange), and Ge (green) interstitials. The population of the phonon modes in Si-I-X systems is slightly affected in the ∼15 THz region.

In order to analyze the propagating character of these phonons, we computed phonon group velocities, $v_\lambda(\mathbf{q})$, from the gradient of frequency $\omega_\lambda(\mathbf{q})$ with respect to wavevector $\mathbf{q}$, i.e., $v_g = v_\lambda(\mathbf{q}) = \partial\omega_\lambda(\mathbf{q})/\partial\mathbf{q}$. Phonon group velocity is a dominant factor in the TC expression [Eq. (9)] and hence can help us to make a qualitative prediction of TC of the material. In Fig. 7, we show the phonon group velocities in Si-I-C (blue), -Si (orange), and -Ge (green) systems, along the symmetry direction [000]-[100] of the supercell in comparison with bulk (black). We find that phonon group velocities above 3–5 THz are greatly decreased in defected systems (∼1 order of magnitude) with respect to those in bulk crystalline Si, due to the presence of interstitials. In fact, the suppression of group velocities has a direct correspondence with the TC decrease trend (Ge < Si < C), as illustrated by our MD simulations (see Fig. 4). As can be noted from Fig. 7, the v_g values in between 3–5 THz are least suppressed in Si-I-C systems, when compared with Si-I-Ge systems. The group velocities of Si-I-Si and Si-I-Ge have a similar profile yielding similar TC values. The inset of Fig. 7 shows the phonon group velocities along the symmetry direction [000]-[100] in Si-I-Ge systems with uniform (magenta) and random (green) distribution of interstitials. The group velocity profile of the Si-I-Ge-random system is lower than the corresponding system with uniform

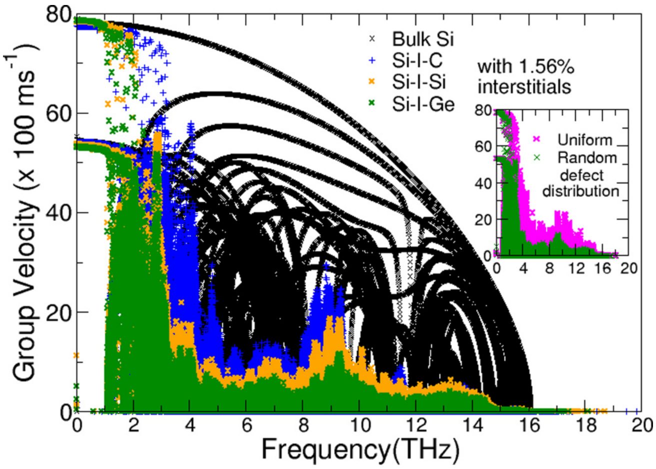

FIG. 7. Phonon group velocities of bulk silicon with 1.56% C (blue), Si (orange), and Ge (green) interstitials compared to bulk (black). Phonon group velocities are strongly reduced in the Si-I-X systems above 3–5 THz and the v_g profile is approximately of the order Ge < Si < C. Inset: Phonon group velocities of Si-I-Ge systems with uniform (magenta) and random (green) distribution of interstitials. Group velocities are more suppressed in Si-I-Ge system with randomly distributed interstitials.

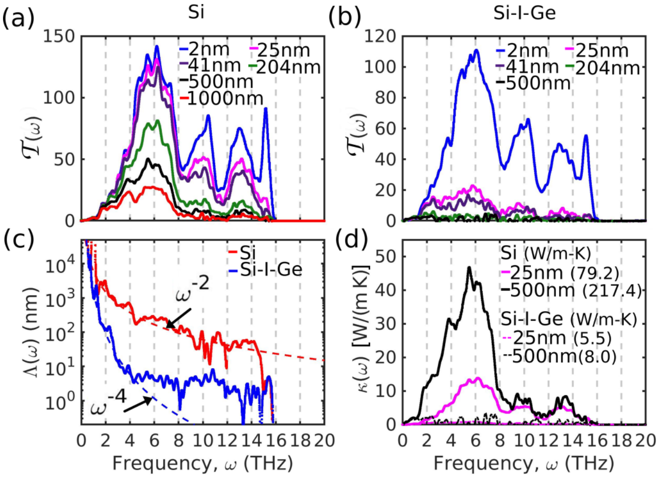

FIG. 8. Length-dependent phonon transmission functions of (a) bulk Si and (b) Si-*I*-Ge with 1.56% Ge interstitials at 300 K, as a function of frequency. The lengths of the samples are indicated by the legends. (c) Phonon mean-free paths in bulk Si (red) and bulk silicon with 1.56% Ge interstitials (blue), evaluated from the length-dependent transmission functions in (a). (d) Representative spectral thermal conductivities of bulk Si (solid lines) and 1.56% Si-*I*-Ge (dashed lines). Reduced phonon transmission and MFPs result in strongly reduced TC of Si-*I*-Ge for all $\omega > 1.5$ THz. The integrated values of TCs are shown within parentheses, next to the legends.

distribution of Ge interstitials, yielding a ~2-fold reduced TC, as reported in Table I.

D. Phonon properties: Transmission and mean-free path

The analysis of phonon group velocities provides a qualitative estimate of the suppression of phonon propagation due to scattering from interstitial defects. In order to characterize phonon scattering in the presence of interstitials, we compute frequency-dependent phonon transmission, $\mathcal{T}(\omega, L)$, and phonon mean-free paths, $\Lambda(\omega)$, in bulk Si with Ge interstitials. $\mathcal{T}(\omega, L)$ of bulk Si and Si-*I*-Ge with 1.56% Ge at room temperatures are shown in Figs. 8(a) and 8(b), respectively. Phonon transmission functions provide highly valuable insight regarding the nature of the scattering mechanisms present and their role in heat transport. For example, the length dependence of the transmission functions illustrates the role of anharmonic scattering in dictating the crossover between the ballistic and the diffusive phonon transport regimes [65]. As can be noted from Fig. 8(a), phonon transmission in bulk Si decreases as a function of the sample length for frequencies higher than 1.5 THz, due to anharmonic scattering. On the other hand, the transmission function is length independent in the low-frequency range, indicating that ballistic transport persists for phonons below 1.5 THz, even in the 1 μm sample. By comparing the length dependence of the spectral phonon transmission in Si-*I*-Ge with that in bulk Si, we evaluate the qualitative effect of scattering on thermal transport introduced by Ge interstitials. $\mathcal{T}(\omega, L)$ of Si-*I*-Ge is remarkably reduced at high frequencies due to the presence of only 1.56% Ge interstitials [Fig. 8(b)], compared to bulk Si of the same length. This observation strengthens our previous conclusion about reduced phonon group velocities and transport above 3–5 THz, in the presence of interstitials. However, $\mathcal{T}(\omega, L)$ does not change with length below 1.5 THz implying that transport remains ballistic. Additionally, it can be seen that the spectral transmission functions of 2 nm Si [Fig. 8(a), blue] and 2 nm Si-*I*-Ge [Fig. 8(b), blue] systems are very similar. We attribute this to the fact that confinement effects play a stronger role in decreasing TC than scattering from point defects in very small systems. To further quantify the impact of interstitials on phonon propagation, we computed the frequency-resolved phonon MFPs from the length-dependent phonon transmission functions, assuming diffusive transport [65]. The computed MFPs, $\Lambda(\omega)$, are not mode resolved.

Figure 8(c) shows the phonon MFPs of bulk Si and Si-*I*-Ge, calculated from the spectral transmission functions. The MFPs, $\Lambda(\omega)$, for each ω are evaluated by fitting the transmission functions of different length systems, which are averaged over 20 data sets, as described in the "Method" section. MFPs of bulk Si for $\omega \leqslant 12$ THz are evaluated by fitting the transmission functions of 2 nm and 1000 nm systems and, for $\omega > 12$ THz, the transmission functions of 2 nm and 41 nm systems. Similarly, MFPs of Si-*I*-Ge for $\omega \leqslant 2.5$ THz are evaluated from the 41 nm and the 500 nm systems and, for $\omega > 2.5$ THz, from the transmission functions of 2 nm and 41 nm systems. The MFPs of bulk Si [Fig. 8(c), red] are proportional to ω^{-2} in the whole frequency range (best fit described by power $\omega^{-1.80}$), as a consequence of phonon-phonon scattering [68,103,104]. In the presence of 1.56% Ge interstitials, MFPs are about 50 times smaller for 2 THz $< \omega <$ 10 THz. Above 5 THz, MFPs of Si-*I*-Ge are even shorter than 5 nm, contributing very little to TC. In contrast, MFPs are quite similar for bulk Si and Si-*I*-Ge for frequencies less than 1.5 THz and are not affected by the presence of interstitials. These phonons can travel long distances without being scattered, even in defected systems. We fitted the MFPs below 5 THz, since the previous analysis showed that phonons with frequencies beyond 5 THz almost do not contribute to the total TC. We found that our best fit is described by power $\omega^{-3.83}$, in accordance with kinetic theory. The power indicates that phonon-defect scattering dictates thermal transport in Si-*I*-Ge, as expected [102].

Finally, we compute the spectral decomposition of TC, $\kappa(\omega)$, to illustrate the role of phonon-defect scattering on thermal transport. Figure 8(d) shows the spectral decomposition of TCs of bulk Si and Si-*I*-Ge, for 25 nm and 500 nm systems. Spectral TCs of the systems in the ballistic regime ($\omega <$ 1.5 THz) are nearly unaffected by the inclusion of interstitials, for any given length. $\kappa(\omega)$ of Si-*I*-Ge is strongly reduced beyond this frequency range. As size increases, scattering plays a greater role in decreasing TCs. These observations are directly supported by the large decrease in phonon transmission in Si-*I*-Ge [Fig. 8(b)] as compared to bulk Si [Fig. 8(a)]. We also report the integrated values of spectral TCs of these systems in Fig. 8(d), within parentheses, next to the system length legends. Although we implemented the harmonic approximation to reduce computational cost, this approximation has been demonstrated to provide a good estimate for thermal properties of Si/Ge superlattices [85]. We verify the effect of employing harmonic force constants on the predicted TC, by comparing the integrated spectral TC with the TC calculated from fully anharmonic heat flux data, recorded during the NEMD simulations. Across all sizes, the integrated spectral TC differs from the fully anharmonic NEMD TC by less than 8%. The converged value of the integrated spectral TC of Si-I-Ge [8 W/(m K)] further matches closely with the TC computed from EMD simulations. We acknowledge that accurately predicting bulk Si TC employing NEMD requires simulating structures greater than 3 μm, 3 times longer than our largest system [105]. We approximated the converged NEMD Si TC value, by extrapolating the linear fit of $1/L$ vs $1/\kappa$ of systems with lengths 204 nm, 500 nm, and 1000 nm [82,106]. We predict a converged Si NEMD TC of 256 W/(m K). This method overpredicts bulk Si TC compared to the TC obtained from EMD simulations, by ~30% [82]. However, it is known that Si TC calculated from NEMD depends on both the cross section and length of the supercell used [82]. Considering the length and cross section of our NEMD structures, we conclude this value is in reasonable agreement with the literature.

E. Electronic transport

In this section, we illustrate the effect of different interstitials in varied lattice symmetry positions on electronic transport properties of Si. The drastic reduction of TC of bulk silicon with the introduction of interstitials makes this a promising materials engineering strategy for thermoelectric applications. However, in order to achieve a high figure of merit (ZT) and attain the phonon-glass-electron-crystal regime, it is important to not only decrease TC but to simultaneously maintain a high power factor (PF). Previous studies with semiempirical and first-principles methods demonstrated that the energetically stable interstitial sites in bulk silicon are of hexagonal, tetrahedral, split-interstitial, and bond-centered type (see Fig. 2) [29,30,33,39,40,42,43,45,46]. Si and Ge interstitial defects are reported to be most stable in the [110] split configuration with formation energies 3.27 eV and 2.25 eV, respectively [40]. The other two stable configurations discussed are hexagonal and tetrahedral. Hexagonal, split (also referred to as dumbbell [110]), and tetrahedral configurations are argued to be the most likely positions Ge atoms occupy while diffusing through Si [33], although this study found the tetrahedral configuration to be unstable. Using an empirical classical potential, the equilibrium configuration for the C interstitial was found to be in the [100] split site with the formation energy of 4.6 eV [44]. The tetrahedral site is shown to be the most stable position for Li interstitials with binding energy of 1.36 eV [45]. We computed the charge transport properties of the Si-I-X systems (X = Ge, C, Si, or Li) with interstitials in each of these above mentioned energetically stable sites. Table II displays the total energies of the Si-I-X systems computed with DFT, with specific atom species X (listed in the leftmost column) in varied interstitial sites of Si. We assigned a reference value (0.00 eV) to the lowest energy across each row and presented the energies in the neighboring columns in the same row with respect to this reference. The split-interstitial sites in Si-I-Si (and -Ge) and Si-I-C systems are considered to be along the [110] and [100] cubic lattice symmetry directions, respectively. The results displayed in Table II indicate that split interstitials are the most energetically favorable sites in Si-I-Si, -Ge, and -C systems, while Li atoms are more stable in tetrahedral sites at 0 K. These results are in good agreement with the conclusions from other theoretical studies, about the stable sites of Ge, C, Si, and Li interstitials in bulk Si.

TABLE II. Total energies of 65-atom Si-I-X supercells with different interstitials in varied sites. The lowest energy across each row is assigned to be the reference and the energies in other columns along the same row are presented with respect to the reference. Empty cells represent systems that are either unstable or have total energies higher than 1 eV from reference. Underlined italic and nonitalic values correspond to systems with semiconductor-like and metal-like behavior, respectively.

Interstitial atom (X)	Total energies of Si-I-X systems (eV) Interstitial site: Bond-centered	Hexagonal	Split	Tetrahedral
Si [29,30,39,40]		$\underline{\mathit{0.07}}$	$\underline{\mathit{0.00}}$	0.20
Ge [33,40]		$\underline{\mathit{0.29}}$	$\underline{\mathit{0.00}}$	0.25
C [42,43]	$\underline{\mathit{0.93}}$	$\underline{\mathit{0.44}}$	0.00	
Li [45,46]		0.51		0.00

However, our MD studies reveal that interstitials are highly likely to access different sites due to temperature fluctuations. Therefore, it is safe to assume that all the sites with energy values reported in Table II are equally probable due to temperature fluctuations and random defect distributions in a sample. We decided to compute charge transport properties of only the systems that are stable and have total energies within 1 eV compared to the most energetically favorable system in the same row. The systems represented by the empty cells in Table II did not satisfy these criteria and therefore were omitted from further investigation. Some of the stable Si-I-X systems exhibited semiconductor-like behavior (underlined italic values) while other exhibited metal-like behavior (nonitalic values). We discuss the properties of the semiconductor-like systems in the next paragraphs followed by the metal-like systems.

To illustrate the role of the different interstitials on charge transport, we calculate the transport coefficients S, σ, κ_e and the power factor ($S^2\sigma$) as functions of the carrier concentration, n_e, and compare with the corresponding values of bulk silicon. Figure 9 shows the electronic transport coefficients of bulk Si and the semiconductor-like Si-I-X systems (underlined italic values in Table II) at 300 K, for the n-doping case. The computed electrical conductivity of bulk Si is in good agreement with experimental data [107]. The Seebeck coefficient, however, is underestimated due to the fact that we do not include the effect of phonon drag in our model. At low carrier concentration, $n_e \sim 10^{16}$ cm^{-3}, the calculated Seebeck coefficient is 870 μV/K, approximately 30% lower than the experimental value, 1250 μV/K [108]. However, we mainly discuss electronic transport properties of highly doped Si-I-X systems, in this study. At such doping, the strong electron-phonon scattering rate decreases the phonon drag contribution to transport. Subsequently, we note that the computed Seebeck coefficient at higher carrier concentration, of $\sim 3 \times 10^{19}$ cm^{-3}, is 220 μV/K, only about 12% lower than the experimental value, 250 μV/K. Since we do not

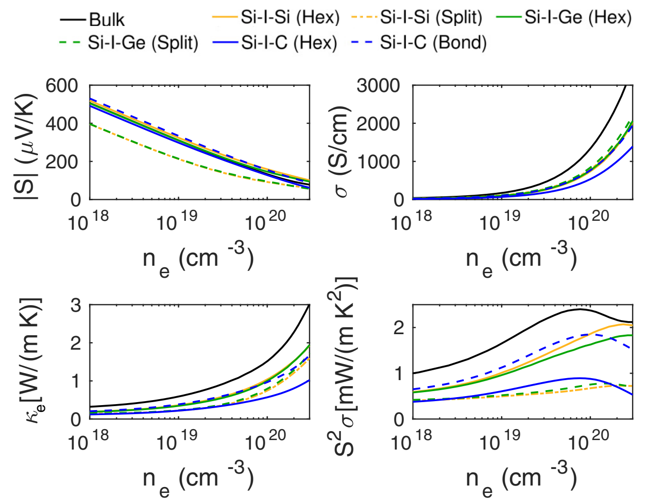

FIG. 9. Calculated Seebeck coefficient, electrical conductivity, electronic thermal conductivity, and power factor of bulk Si and bulk Si-I-X systems.

include the phonon drag effect in any of our calculations, we argue that comparison within our computed results is justified due to the same level of systematically implemented approximation.

As can be seen from Fig. 9, the transport coefficients are significantly altered due to the presence of the interstitials. Both Si-I-Si and -Ge systems with split interstitials have a smaller S compared to bulk Si, while other interstitials leave S relatively unaltered. Introduction of the interstitials consistently decreases both σ and κ_e. All Si-I-X systems except Si-I-C-hexagonal have similar values of the conductivities; a hexagonal C interstitial yields the lowest σ and κ_e. The combination of S and σ yields a small PF for the Si-I-C-hexagonal system as well as Si-I-Si and -Ge systems with split interstitials. However, the power factors of Si-I-Si and Si-I-Ge approach the power factor of bulk silicon at high carrier concentrations. The electronic transport coefficients were evaluated within the framework of semiclassical Boltzmann transport theory [68] as expressed in Eqs. (5)–(8). Therefore, it is essential to examine the factors in the argument of the integral in Eq. (5), for a complete understanding of the effect of interstitials on the charge transport coefficients.

In the following, we discuss the details of the electronic band structures and the density of states (DOS) that determine the transport coefficients. The left panel of Fig. 10 shows the band structures of the semiconductor-like Si-I-X systems (underlined italic values in Table II). All interstitial impurities introduce additional levels within the energy band gap. The levels close to the band edges (either conduction band minimum or valence band maximum) are referred to as "shallow" levels and those far away from the band edges as "deep" levels [69]. The band structures of Si-I-Si [panel (a)] and -Ge [panel (b)] are very similar. Interstitials in hexagonal sites in these two systems introduce two deep levels in the valence zone and few shallow levels in the conduction zone. The same species in the split-interstitial sites create two deep levels in the valence zone with one deep and a few shallow levels in the conduction zone. It is known that the energy gap computed from Kohn-Sham states is systematically underestimated [109]. However, it does not affect the calculation of transport coefficients because we only study transport properties of highly doped n-type materials; therefore, the integrations in Eqs. (5)–(8) are performed over the energy bands in the conduction zone. The deep levels in the conduction zone decrease transport coefficients due to the $\partial f/\partial\epsilon$ factor in the integrand as shown in Eq. (5). In general, deep levels lead to poor electron (hole) transport properties because of the low density of available states in the region close to the conduction

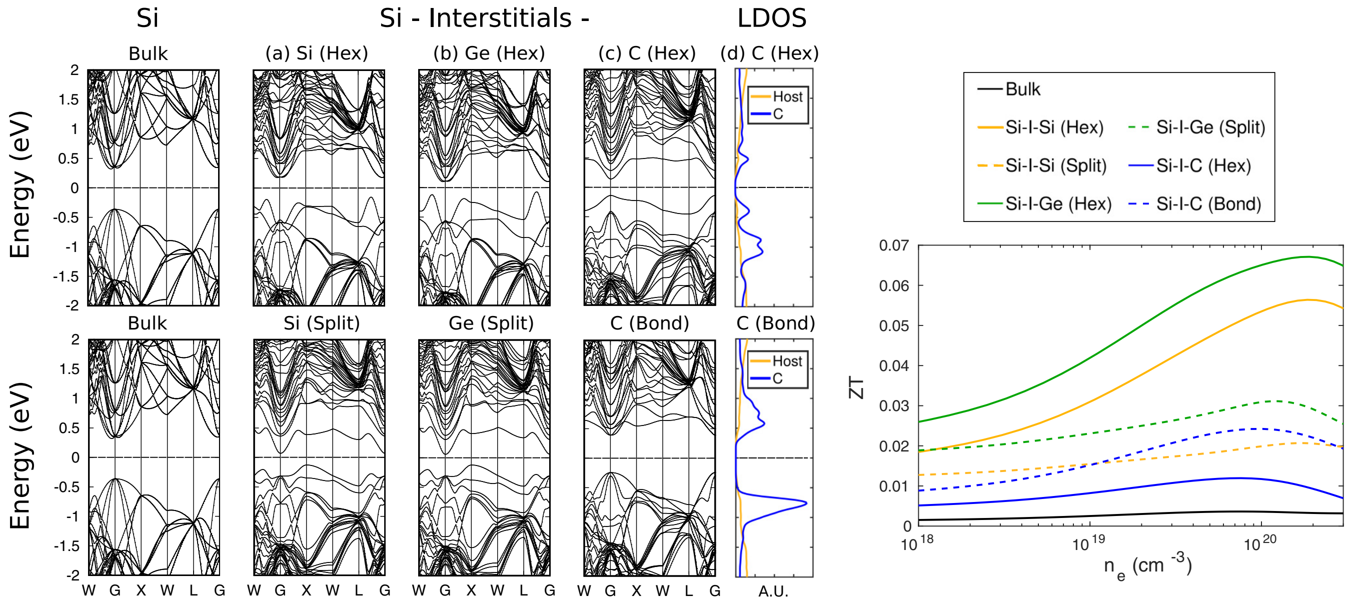

FIG. 10. Left panel: Band structures of bulk Si and semiconductor-like Si-I-X systems (Underlined italic values in Table II). Middle panel: The local density of states (LDOS) of Si-I-C with C interstitial in the bond-centered and the hexagonal sites. The Fermi level is chosen to be at 0 eV for all cases. Right panel: Figure of merit (ZT) of semiconductor-like Si-I-X systems compared to that of bulk Si.

(valence) zone edge (see Fig. 10). That is the reason the hexagonal interstitials induce better charge transport in the n-type Si-I-Si(-Ge) (Fig. 9 [solid orange (green) line]) rather than the split-interstitials (Fig. 9 [orange (green) dashed line]). On the other hand, C interstitials in hexagonal sites introduce one deep level in both the valence and the conduction zones [panel (c), top]. The deep level in the conduction band leads to poor transport properties as shown in Fig. 9 (blue solid line). Interestingly, C interstitials in bond-centered positions do not add any deep levels within the band gap [panel (c), bottom] and yield better transport properties [Fig. 9 (blue dashed line)].

In order to understand the origin of the deep and the shallow levels, we compute the local density of electronic states (LDOS) of Si-I-C systems, shown in Fig. 10, panel (d). LDOS describes the space-resolved electronic density of states, which is computed using the postprocessing "projwfc.x" code available through the QE package. LDOS allows us to quantify the contributions from interstitial and host atoms separately to the full electronic density of states of the system. Figure 10 [panel (d), top] shows the comparison between the density of states contributed by the C interstitial (blue) and the host Si atoms (normalized by the number of Si atoms) (orange). The peaks in the LDOS illustrate that C interstitials primarily contribute to the additional deep and the shallow levels, in both hexagonal and bond-center sites. The two peaks [panel (d), top, blue] in LDOS close to the Fermi level correspond to the deep levels in band structure in Si-I-C-hexagonal systems, while two distinguished peaks ∼0.5 and ∼0.7 eV [panel (d), bottom, blue] are directly related to the shallow levels in the Si-I-C-bond-centered systems.

We obtained the thermoelectric figure of merit ZT of the Si-I-X systems at 300 K (Fig. 10, right panel) by combining the electronic transport coefficients with our MD κ_{ph} results, shown in Fig. 4. Since κ_{ph} is strongly suppressed in the presence of the interstitials, we see a significant improvement of ZT for all Si-I-X systems studied in this work compared to bulk Si. The highest ZT are obtained for Si-I-Si and -Ge-hexagonal systems due to a combination of low κ_{ph}'s and high PFs. 1.56% of Ge interstitials in the hexagonal sites are found to improve ZT of bulk Si by a factor of 17. The lowest ZT value is found to be for Si-I-C systems with interstitials in the hexagonal sites. Even for this case the figure of merit is 3 times larger than the reference bulk value [110].

As we illustrated in the preceding text, interstitials introduce additional energy levels in the band structure. Both the deep and the shallow levels lead to smaller energy gaps of the Si-I-X systems. We now turn our attention to the systems marked with nonitalic values in Table II. The interstitials not only shrink the energy band gaps of these systems but greatly alter the electronic properties rendering them metal-like. In Fig. 11 we present the band structures of the metal-like Si-I-X systems (nonitalic values in Table II): Si-I-Si, -Ge, and -Li in the tetrahedral sites and -C in the split-interstitial sites. (The interstitial configurations are as depicted in Fig. 2.) In the Si-I-Si(-Ge or -Li)-tetrahedral systems [panels (a), (b), and (e)] the energy gap is minimally altered but the Fermi level is shifted so that it intersects the conduction bands—such behavior resembles the band structures of highly doped n-type semiconductors. The band structures of Si-I-Si and Si-I-Ge in tetrahedral positions [panels (a) and (b)] are rather similar. The interstitials not only shift the Fermi level but introduce additional shallow energy levels in the conduction zone. In comparison, Li interstitials do not create any additional levels near the conduction band edge [panel (e)]. However, the Fermi level is shifted to the conduction zone indicating metal-like behavior similar to Si-I-Si and -Ge in tetrahedral sites. We found no significant difference in the band structures between Si-I-Li-tetrahedral and -hexagonal systems. In order to avoid redundancy, we refrain from displaying the Si-I-Li-hexagonal band structure in this article. The Si-I-C-split-interstitial system exhibits a combined effect of smaller energy gap due to additional deep energy levels (similarly to the Si-I-C-hexagonal system shown in Fig. 10) and shifted Fermi level leading to metal-like characteristics.

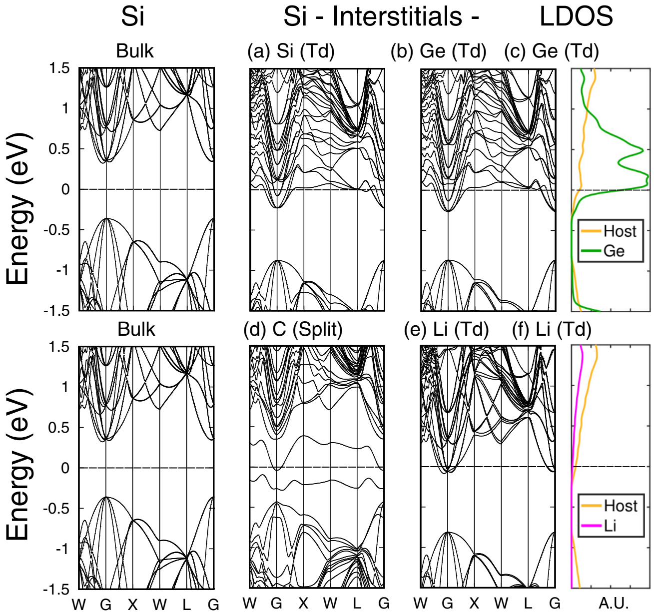

FIG. 11. Band structures of bulk Si and metal-like Si-I-X systems (nonitalic values in Table II). The plots in the rightmost panels represent the local density of states (arbitrary units) of (c) Si-I-Ge-tetrahedral and (f) Si-I-Li-tetrahedral systems. The Fermi level is chosen to be at 0 eV for all cases.

We present the LDOS of the metal-like Si-I-X systems in the rightmost panel of Fig. 11 to discuss the origin of these additional bands. Comparison between the LDOSs of the Si-I-Ge and Si-I-Li tetrahedral systems [panels (c) and (f)] shows that Ge interstitials (green) are responsible for creating shallow energy levels in ~ -0.2 to 1 eV range. Additionally, we analyzed the projected density of states in Si-I-Ge tetrahedral system, and found that the additional conduction bands created are mostly formed from the p electrons of the guest atom. In contrast, Li interstitials (magenta) do not create distinct peaks either in conduction or valence zones. This can be explained by the fact that Li has fewer electrons than Ge and Si atoms. For the same reason, Li interstitials do not affect the band structure significantly. The orange curves in Fig. 11 represent the contribution of host atoms to the DOS, scaled with respect to the total number of Si atoms. These results indicate that interstitials offer a viable strategy

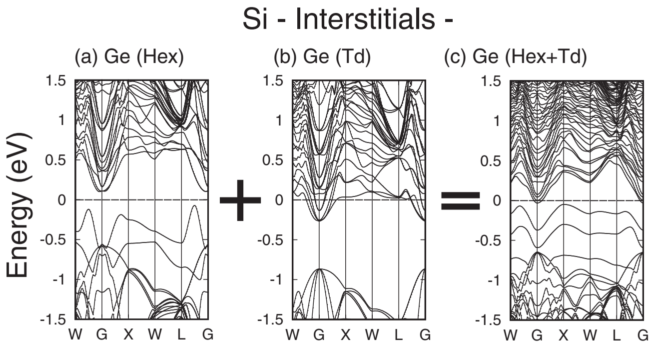

FIG. 12. Band structures of Si-I-Ge systems with interstitials located in (a) hexagonal, (b) tetrahedral, and (c) both hexagonal and tetrahedral sites. The Fermi level is chosen to be at 0 eV for all cases.

to design n-type semiconductors without explicit dopants, e.g., substitutionally doped bulk silicon with pentavalent impurities such as phosphorus.

We acknowledge that in experimental samples the interstitial atoms are likely to reside in different symmetry positions (e.g., hexagonal, tetrahedral) within the crystal due to the variability of the neighbor-bonding environment and temperature fluctuations. In order to simulate an experimentally realizable system, we investigate the electronic properties of a Si-I-X system containing interstitial atoms in different symmetry sites. The system consists of 128 Si host atoms and 2 Ge interstitials, one in the hexagonal and the other in the tetrahedral symmetry position. Thus we maintain a 1.56% concentration of interstitials within bulk, consistent with the cases discussed thus far. In Fig. 12 we present the band structures of Si-I-Ge (a) -hexagonal, (b) -tetrahedral, and (c) -combination of hexagonal and tetrahedral configurations. As can be noted, the combined system [panel (c)] preserves features from both individual cases [panels (a) and (b)]. The hexagonal Ge interstitial introduces two additional levels in the energy gap closer to the valence band edge and additional shallow levels in the conduction zone [panels (a) and (c)], while tetrahedral Ge shifts the Fermi level to the conduction zone and introduces additional shallow energy levels in the conduction zone [panels (b) and (c)]. To calculate the figure of merit of the Si-I-Ge system with interstitials placed in both hexagonal and tetrahedral positions [panel (c)], we calculate transport coefficients at the Fermi level. Combining results obtained from the electronic transport calculations with our Si-I-Ge κ_{ph} results, we find the figure of merit to be 0.01.

F. Structure-ZT map

We now combine the previously computed phonon and electron transport properties to establish a structure-processing-figure-of-merit map of silicon, in the presence of interstitial defects.We present a comprehensive illustration of the variability of ZT of Si-I-X systems in Fig. 13, by combining the electronic transport coefficients with our MD results of κ_{ph}. The x, y, and z axes represent interstitial site type in bulk Si, guest species type, and ZT, respectively. The top panel (a) displays ZT values of n-doped bulk Si systems with interstitials in different symmetry sites. The carrier concentration is chosen such that the ZT value is optimal. All the systems exhibit higher ZT than bulk Si, which peaks at ~0.004, computed with a similar method [110]. The highest ZT value was found for Si-I-Ge-hexagonal systems with ZT approaching ~0.067, which is 17 times larger than the reference bulk value. The lowest ZT value ~0.012 was obtained for the Si-I-C system with interstitials in the hexagonal sites. Even for this case the figure of merit is 3 times larger than the reference bulk value. The bottom panel (b) shows ZT of Si-I-X systems with metal-like character. The figure of merit was obtained from the transport coefficients calculated at the Fermi level. The most improved ZT for metal-like systems was found for the Si-I-Li-tetrahedral system with ZT value of ~0.047. The system with C interstitials in split positions yields the lowest ZT value of ~0.0003, which is 10 times lower than the bulk value. We obtained these values employing an assumption that small (~1%) concentration of interstitials does not affect the electron relaxation times significantly and, therefore, used the scattering time reported for bulk silicon [99,100] (see "Method" section for details). We further assume that electron relaxation time is independent of symmetry position and atom type of the defects, and depends on the defect concentration only. Within this assumption, we believe that our conclusion about the relative impact of different configurations on ZT remains valid, even if the relaxation time or the mobility of electronic carriers in bulk Si is reduced in the presence of 1.56% interstitial defects. In that case, the overall impact of all configurations studied will be scaled by the appropriate factor.

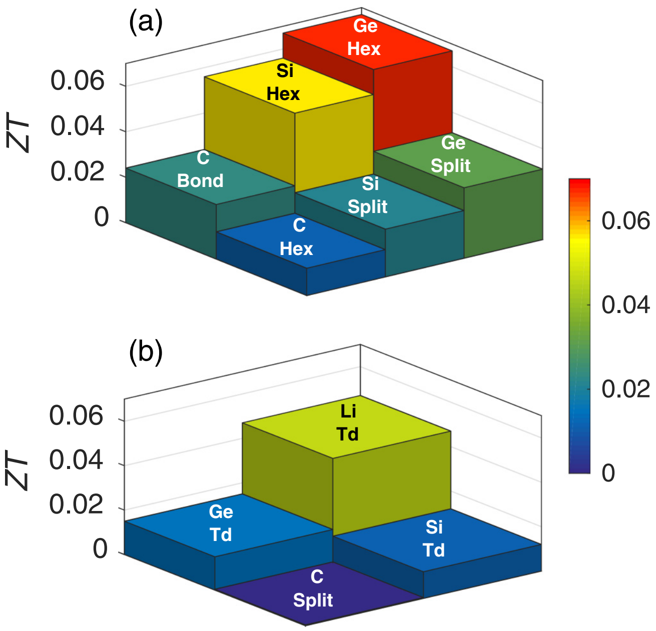

FIG. 13. Variability of thermoelectric figure of merit ZT of bulk Si with interstitials, as a function of the guest atom type and its symmetry position in the lattice.

IV. SUMMARY

In summary, we performed a systematic study of the effect of naturally occurring randomly distributed interstitial defects (Si, Ge, C, and Li) [33,35,44,48,50] on the charge and heat transport properties of bulk silicon, using first-principles DFT and atomistic lattice dynamics and MD techniques, respectively. Our atomistic modeling, using empirical potentials, reveals that interstitial defects do not significantly alter the phonon density of states. However, the group velocities, phonon transmission and MFPs, and therefore the propagation of phonons, are strongly suppressed. Previous studies only incorporated isolated interstitials interacting with simplified neighbor forces [60]; therefore, the results cannot be compared with our study performed with large systems incorporating randomly distributed defects. The reduction of group velocities follows the trend Ge $<$ Si $<$ C, leading to a decrease in the TCs following the same order: Si-I-Ge $<$ -Si $<$ -C, with Ge having the most and C the least impact in lowering the TC. The influence of defect scattering on propagation is further reflected by the phonon MFPs. In the presence of 1.56% Ge interstitials, MFPs are about 50 times smaller in the 2 THz $< \omega <$ 10 THz region, compared to those of bulk Si. Above 5 THz, MFPs of Si-I-Ge are even shorter than 5 nm, contributing very little to TC. We report modification of phonon MFPs in large experimentally realizable Si systems in the presence of randomized interstitial defects. We show the implementation of a newly developed NEMD-based method to verify Rayleigh scattering by interstitial defects. Li interstitials are diffusive in character leading to significant disorder in the lattice. This is likely to be the reason for Li interstitials to lower bulk Si TC the most. Randomly dispersed 1.56% Li, Ge, Si, and C interstitials decrease the TC of bulk Si by $\sim$ 34, 30, 20, and 9 times, respectively. This result suggests that interstitials offer a viable approach to achieve controlled phonon scattering, due to the tunability of mass and size of the guest atom, and thereby achieve a phonon-glass paradigm to engineer next-generation thermoelectric materials.

In parallel, we investigated the electronic transport properties of bulk Si with 1.56% neutral Ge, C, Si, and Li interstitials in hexagonal, tetrahedral, split-interstitial, and bond-centered sites. Our investigation is among the few studies reported that calculated electronic transport properties with interstitial point defects. We demonstrate that Si and Ge in the hexagonal sites minimally impact the charge transport properties of bulk silicon. This combined with the decreased values of κ_{ph} leads to 14 and 17 times improved thermoelectric figures of merit without introduction of explicit dopants, respectively. These values were calculated with an assumption that a small ($\sim$1%) concentration of interstitials does not affect the electron relaxation times significantly, and therefore we used the scattering times reported for bulk silicon [99,100]. Our results illustrate that electronic transport in defected systems strongly depends on the symmetry positions of defects in the lattice. For example, the bonding environment of split Ge interstitials is marked with the smallest first-NN distance 2.3 Å (obtained from DFT relaxation). The LDOSs reveal that the interstitials introduce two deep levels in the valence zone and one deep and few shallow levels in the conduction zone. The deep level (conduction) leads to reduced charge transport properties compared to pristine bulk Si. In comparison, Ge in a hexagonal site, bonded with the first NN at a distance 2.43 Å, introduces two deep levels in the valence zone and only shallow levels in the conduction zone. The shallow levels result in a better charge transport. A tetrahedral Ge interstitial, on the other hand, pushes host NN silicon atoms farther away to a distance 2.5 Å, yielding a shifted Fermi level resembling a highly doped n-type semiconductor. When the Ge interstitial is loosely bound to its first NN, it tends to create additional shallow energy levels. A tightly bound split interstitial leads to deep levels in the band structure that diminishes electron transport. This qualitative understanding, however, may not be generalized to all defects.

We acknowledge that it may not be possible to control the symmetry locations of the interstitials in an experimental sample. We compute the properties of an experimentally realizable silicon system, consisting of both a hexagonal and a tetrahedral Ge interstitial defect. We illustrate that the defects in this system display an additive behavior: the Fermi level is shifted (characteristic of a tetrahedral Ge) as well as additional shallow levels are introduced in the conduction zone (due to hexagonal Ge). Our modeling data furnish indirect measures to estimate the presence of interstitial defects in a sample, from the measured thermal and electronic properties of the system. For example, the electronic DOS can be measured with STM techniques [111]. The observed band gap and the presence of deep/shallow levels in the STM data can be compared with our theoretical results, to estimate the defects present in the system. We believe that this study further provides with an important step toward addressing the long outstanding problem—to determine the role interstitials play in mediating various diffusion mechanisms in doped semiconductors, fabricated with standard techniques, as well as radiation damaged silicon in space applications. Our research establishes a direct relationship between the variability of structures dictated by fabrication processes and heat and charge transport properties, and allows us to accurately predict performance of Si-based materials for various technological applications. We envision that the processing-structure-transport (heat and charge) property map will enable further developments of silicon-based materials with predictable, robust, and optimal performance.

ACKNOWLEDGMENTS

We are indebted to Shiyun Xiong for useful discussions and assistance with phonon transmission calculations. We thank Björn Baumeier for useful discussions and Paul F. Salame for his work preparing defected structures for MD. This work is funded by the DARPA (DSO) MATRIX program [Agreement No.: HR0011-16-2-0043]. This work used the Extreme Science and Engineering Discovery Environment (XSEDE), which is supported by National Science Foundation Grant No. ACI-1548562. We are grateful for the computing resources provided by the Department of Defense (DoD) High Performance Computing Modernization Program (HPCMP) at the Air Force Research Laboratory DoD Supercomputing Research Center (AFRL-DSRC). We acknowledge the computing resources provided the RMACC Summit supercomputer, which is supported by the National Science Foundation (Awards No. ACI-1532235 and No. ACI-1532236), the University of Colorado Boulder, and Colorado State University. The Summit supercomputer is a joint effort of the University of Colorado Boulder and Colorado State University.

[1] G. Pacchioni, L. Skuja, and D. L. Griscom, *Defects in* SiO_2 *and Related Dielectrics: Science and Technology*, Vol. 2 (Springer Science & Business Media, 2012).

[2] G. Ribes, J. Mitard, M. Denais, S. Bruyere, F. Monsieur, C. Parthasarathy, E. Vincent, and G. Ghibaudo, IEEE Trans. Device Mater. Reliab. **5**, 5 (2005).

[3] J. S. Park, W.-J. Maeng, H.-S. Kim, and J.-S. Park, Thin Solid Films **520**, 1679 (2012).

[4] G. D. Wilk, R. M. Wallace, and J. Anthony, J. Appl. Phys. **89**, 5243 (2001).

[5] L. L. Baranowski, P. Zawadzki, S. Lany, E. S. Toberer, and A. Zakutayev, Semicond. Sci. Technol. **31**, 123004 (2016).

[6] F. Scholz, Semicond. Sci. Technol. **27**, 024002 (2012).

[7] J. A. Weil, Phys. Chem. Miner. **10**, 149 (1984).

[8] F. Jelezko and J. Wrachtrup, Phys. Status Solidi A **203**, 3207 (2006).

[9] L. Rondin, J. Tetienne, T. Hingant, J. Roch, P. Maletinsky, and V. Jacques, Rep. Prog. Phys. **77**, 056503 (2014).

[10] C. Wadia, A. P. Alivisatos, and D. M. Kammen, Environ. Sci. Technol. **43**, 2072 (2009).

[11] G. J. Snyder and E. S. Toberer, Nat. Mater. **7**, 105 (2008).

[12] X. Shi, L. Chen, and C. Uher, Int. Mater. Rev. **61**, 379 (2016).

[13] P. Pichanusakorn and P. Bandaru, Mater. Sci. Eng., R **67**, 19 (2010).

[14] A. Shakouri, Annu. Rev. Mater. Res. **41**, 399 (2011).

[15] C. J. Vineis, A. Shakouri, A. Majumdar, and M. G. Kanatzidis, Adv. Mater. **22**, 3970 (2010).

[16] J.-F. Li, W.-S. Liu, L.-D. Zhao, and M. Zhou, NPG Asia Mater. **2**, 152 (2010).

[17] S. E. Thompson, M. Armstrong, C. Auth, M. Alavi, M. Buehler, R. Chau, S. Cea, T. Ghani, G. Glass, T. Hoffman *et al.*, IEEE Trans. Electron Devices **51**, 1790 (2004).

[18] S. J. Koester, J. D. Schaub, G. Dehlinger, and J. O. Chu, IEEE J. Sel. Top. Quantum Electron. **12**, 1489 (2006).

[19] J. Liu, X. Sun, R. Camacho-Aguilera, L. C. Kimerling, and J. Michel, Opt. Lett. **35**, 679 (2010).

[20] G. Chen, M. Dresselhaus, G. Dresselhaus, J.-P. Fleurial, and T. Caillat, Int. Mater. Rev. **48**, 45 (2003).

[21] M. S. Dresselhaus, G. Chen, M. Y. Tang, R. Yang, H. Lee, D. Wang, Z. Ren, J.-P. Fleurial, and P. Gogna, Adv. Mater. **19**, 1043 (2007).

[22] H. Alam and S. Ramakrishna, Nano Energy **2**, 190 (2013).

[23] G. Kissinger and S. Pizzini, *Silicon, Germanium, and Their Alloys: Growth, Defects, Impurities, and Nanocrystals* (CRC Press, 2014).

[24] J. R. Srour, C. J. Marshall, and P. W. Marshall, IEEE Trans. Nucl. Sci. **50**, 653 (2003).

[25] A. Haque and S. Sumaiya, J. Manufacturing Mater. Process. **1**, 6 (2017).

[26] G. Dehlinger, S. Koester, J. Schaub, J. Chu, Q. Ouyang, and A. Grill, IEEE Photonics Technol. Lett. **16**, 2547 (2004).

[27] J. Jung, S. Yu, O. O. Olubuyide, J. L. Hoyt, D. A. Antoniadis, M. L. Lee, and E. A. Fitzgerald, Appl. Phys. Lett. **84**, 3319 (2004).

[28] D. Chadi, Phys. Rev. B **46**, 9400 (1992).

[29] R. Needs, J. Phys.: Condens. Matter **11**, 10437 (1999).

[30] W.-C. Lee, S.-G. Lee, and K. Chang, J. Phys.: Condens. Matter **10**, 995 (1998).

[31] W.-K. Leung, R. J. Needs, G. Rajagopal, S. Itoh, and S. Ihara, Phys. Rev. Lett. **83**, 2351 (1999).

[32] P. Rinke, A. Janotti, M. Scheffler, and C. G. Van de Walle, Phys. Rev. Lett. **102**, 026402 (2009).

[33] D. Caliste, P. Pochet, T. Deutsch, and F. Lançon, Phys. Rev. B **75**, 125203 (2007).

[34] R. Aggarwal, P. Fisher, V. Mourzine, and A. Ramdas, Phys. Rev. **138**, A882 (1965).

[35] G. Watkins and K. Brower, Phys. Rev. Lett. **36**, 1329 (1976).

[36] R. Newman, Rep. Prog. Phys. **45**, 1163 (1982).

[37] G. D. Watkins, Mater. Sci. Semicond. Process. **3**, 227 (2000).

[38] J. Bourgoin and M. Lannoo, in *Point Defects in Semiconductors*, Vol. 2: Experimental Aspects, edited by M. Cardona (Springer, 1983).

[39] Y. Bar-Yam and J. D. Joannopoulos, Phys. Rev. B **30**, 2216 (1984).

[40] L. Wang, P. Clancy, and C. S. Murthy, Phys. Rev. B **70**, 165206 (2004).

[41] Y. Shimizu, M. Uematsu, and K. M. Itoh, Phys. Rev. Lett. **98**, 095901 (2007).

[42] G. Watkins, Chin. J. Phys. **15**, 92 (1977).

[43] M. J. Burnard and G. G. DeLeo, Phys. Rev. B **47**, 10217 (1993).

[44] J. Tersoff, Phys. Rev. Lett. **64**, 1757 (1990).

[45] W. Wan, Q. Zhang, Y. Cui, and E. Wang, J. Phys.: Condens. Matter **22**, 415501 (2010).

[46] G. A. Tritsaris, K. Zhao, O. U. Okeke, and E. Kaxiras, J. Phys. Chem. C **116**, 22212 (2012).

[47] H. Kim, K. E. Kweon, C.-Y. Chou, J. G. Ekerdt, and G. S. Hwang, J. Phys. Chem. C **114**, 17942 (2010).

[48] P. M. Fahey, P. Griffin, and J. Plummer, Rev. Mod. Phys. **61**, 289 (1989).

[49] E. Pell, J. Appl. Phys. **31**, 291 (1960).

[50] P. Fahey, S. Iyer, and G. Scilla, Appl. Phys. Lett. **54**, 843 (1989).

[51] C. Zechner and N. Zographos, Mater. Sci. Semicond. Process. **42**, 230 (2016).

[52] A. Willoughby, Rep. Prog. Phys. **41**, 1665 (1978).

[53] G. Joshi, H. Lee, Y. Lan, X. Wang, G. Zhu, D. Wang, R. W. Gould, D. C. Cuff, M. Y. Tang, M. S. Dresselhaus *et al.*, Nano Lett. **8**, 4670 (2008).

[54] X. Wang, H. Lee, Y. Lan, G. Zhu, G. Joshi, D. Wang, J. Yang, A. Muto, M. Tang, J. Klatsky *et al.*, Appl. Phys. Lett. **93**, 193121 (2008).

[55] N. S. Bennett, N. M. Wight, S. R. Popuri, and J.-W. G. Bos, Nano Energy **16**, 350 (2015).

[56] Y. Lee, S. Lee, and G. S. Hwang, Phys. Rev. B **83**, 125202 (2011).

[57] T. Wang, G. Madsen, and A. Hartmaier, Modell. Simul. Mater. Sci. Eng. **22**, 035011 (2014).

[58] D. K. Brice, Phys. Rev. **140**, A1211 (1965).

[59] K. Ohashi and Y. Ohashi, J. Phys. C **9**, 733 (1976).

[60] D. N. Talwar, J. Appl. Phys. **54**, 2366 (1983).

[61] D. Talwar, M. Vandevyver, and K. Bajaj, Phys. Rev. B **36**, 1715 (1987).

[62] L. Bellomonte and M. Pryce, Proc. Phys. Soc. **89**, 973 (1966).

[63] T. Takabatake, K. Suekuni, T. Nakayama, and E. Kaneshita, Rev. Mod. Phys. **86**, 669 (2014).

[64] G. S. Nolas, J. Sharp, and J. Goldsmid, *Thermoelectrics: Basic Principles and New Materials Developments* (Springer Science & Business Media, 2013).

[65] K. Sääskilahti, J. Oksanen, and J. Tulkki, Phys. Rev. E **88**, 012128 (2013).
[66] K. Sääskilahti, J. Oksanen, J. Tulkki, and S. Volz, Phys. Rev. B **90**, 134312 (2014).
[67] K. Sääskilahti, J. Oksanen, S. Volz, and J. Tulkki, Phys. Rev. B **91**, 115426 (2015).
[68] J. M. Ziman, *Electrons and Phonons: The Theory of Transport Phenomena in Solids* (Oxford University Press, 1960).
[69] H. Grimmeiss, Annu. Rev. Mater. Sci. **7**, 341 (1977).
[70] Q. Song, J. Zhou, L. Meroueh, D. Broido, Z. Ren, and G. Chen, Appl. Phys. Lett. **109**, 263902 (2016).
[71] H. Bracht, H. H. Silvestri, I. D. Sharp, and E. E. Haller, Phys. Rev. B **75**, 035211 (2007).
[72] P. G. Coleman and C. P. Burrows, Phys. Rev. Lett. **98**, 265502 (2007).
[73] Y. Bar-Yam and J. D. Joannopoulos, Phys. Rev. B **30**, 1844 (1984).
[74] P. A. Schultz, Phys. Rev. Lett. **96**, 246401 (2006).
[75] B. R. Tuttle and S. T. Pantelides, Phys. Rev. Lett. **101**, 089701 (2008).
[76] F. Murphy-Armando and S. Fahy, Phys. Rev. Lett. **97**, 096606 (2006).
[77] C. Jiang, S. Maloy, and S. Srinivasan, Scr. Mater. **58**, 739 (2008).
[78] J. Tersoff, Phys. Rev. B **39**, 5566 (1989).
[79] Z. Cui, F. Gao, Z. Cui, and J. Qu, J. Power Sources **207**, 150 (2012).
[80] R. Zwanzig, Annu. Rev. Phys. Chem. **16**, 67 (1965).
[81] S. Plimpton, J. Comput. Phys. **117**, 1 (1995).
[82] Y. He, I. Savić, D. Donadio, and G. Galli, Phys. Chem. Chem. Phys. **14**, 16209 (2012).
[83] Y. Chalopin and S. Volz, Appl. Phys. Lett. **103**, 051602 (2013).
[84] M. P. Allen and D. J. Tildesley, *Computer Simulation of Liquids* (Clarendon Press, 1992).
[85] X. Yang and W. Li, Phys. Rev. Mater. **2**, 015401 (2018).
[86] S. Xiong, D. Selli, S. Neogi, and D. Donadio, Phys. Rev. B **95**, 180301 (2017).
[87] Y. Zhou and M. Hu, Phys. Rev. B **95**, 115313 (2017).
[88] E. S. Landry and A. J. H. McGaughey, Phys. Rev. B **79**, 075316 (2009).
[89] J. A. Johnson, A. A. Maznev, J. Cuffe, J. K. Eliason, A. J. Minnich, T. Kehoe, C. M. Sotomayor Torres, G. Chen, and K. A. Nelson, Phys. Rev. Lett. **110**, 025901 (2013).
[90] R. Gereth and K. Hubner, Phys. Rev. **134**, A235 (1964).
[91] A. M. Stoneham, *Theory of Defects in Solids: Electronic Structure of Defects in Insulators and Semiconductors* (Oxford University Press, 2001).
[92] S. T. Pantelides, Rev. Mod. Phys. **50**, 797 (1978).
[93] C. Freysoldt, B. Grabowski, T. Hickel, J. Neugebauer, G. Kresse, A. Janotti, and C. G. Van de Walle, Rev. Mod. Phys. **86**, 253 (2014).
[94] J. P. Perdew, K. Burke, and M. Ernzerhof, Phys. Rev. Lett. **77**, 3865 (1996).
[95] P. Giannozzi, S. Baroni, N. Bonini, M. Calandra, R. Car, C. Cavazzoni, D. Ceresoli, G. L. Chiarotti, M. Cococcioni, I. Dabo *et al.*, J. Phys.: Condens. Matter **21**, 395502 (2009).
[96] H. J. Monkhorst and J. D. Pack, Phys. Rev. B **13**, 5188 (1976).
[97] G. K. Madsen and D. J. Singh, Comput. Phys. Commun. **175**, 67 (2006).
[98] N. W. Ashcroft and N. D. Mermin, *Solid State Physics* (Saunders, Philadelphia, 1976).
[99] C. Jacoboni, C. Canali, G. Ottaviani, and A. A. Quaranta, Solid-State Electron. **20**, 77 (1977).
[100] S. M. Goodnick, *Computational Electronics* (Morgan and Claypool Publishers, 2006).
[101] J. Garg, N. Bonini, B. Kozinsky, and N. Marzari, Phys. Rev. Lett. **106**, 045901 (2011).
[102] P. Klemens, Proc. Phys. Soc. London, Sect. A **68**, 1113 (1955).
[103] J. Callaway, Phys. Rev. **113**, 1046 (1959).
[104] M. Holland, Phys. Rev. **132**, 2461 (1963).
[105] D. P. Sellan, E. S. Landry, J. E. Turney, A. J. H. McGaughey, and C. H. Amon, Phys. Rev. B **81**, 214305 (2010).
[106] P. K. Schelling, S. R. Phillpot, and P. Keblinski, Phys. Rev. B **65**, 144306 (2002).
[107] P. Chapman, O. Tufte, J. D. Zook, and D. Long, J. Appl. Phys. **34**, 3291 (1963).
[108] A. Van Herwaarden, Sens. Actuators **6**, 245 (1984).
[109] J. P. Perdew, Int. J. Quantum Chem. **30**, 451 (1986).
[110] C. Mangold, S. Neogi, and D. Donadio, Appl. Phys. Lett. **109**, 053902 (2016).
[111] A. J. Yost, A. Pimachev, C.-C. Ho, S. B. Darling, L. Wang, W.-F. Su, Y. Dahnovsky, and T. Chien, ACS Appl. Mater. Interfaces **8**, 29110 (2016).